Submitted to Journal of Geophysical Research

Simulating the ice-thickness distribution in a coupled climate model

C.M. Bitz[1], M.M. Holland[2], A.J. Weaver, and M. Eby

School of Earth and Ocean Sciences, University of Victoria, Victoria, Canada

Abstract. Climate simulations in a global coupled model are investigated using a dynamic-thermodynamic sea ice and snow model with sophisticated thermodynamics and a sub-grid scale parameterization for multiple ice thicknesses. In addition to the sea ice component, the model includes a full primitive-equation ocean and a simple energy-moisture balance atmosphere. We introduce a formulation of the ice thickness distribution that is Lagrangian in thickness-space. The method is designed to use fewer thickness categories because it adjusts to place resolution where it is needed most, and it is free of diffusive effects that tend to smooth Eulerian distributions. Experiments demonstrate that the model does reasonably well in simulating the mean arctic climate. We find the climate of the Arctic and northern North Atlantic is sensitive to resolving the ice thickness distribution when comparing the model results to a simulation with a two-level sea ice model. The ice-thickness distribution causes ice export through Fram Strait to be more variable and more strongly linked to meridional overturning in the North Atlantic Ocean.

The Lagrangian formulation of the ice thickness distribution allows for the inclusion of a vertical temperature profile with relative ease compared to an Eulerian method. We find ice growth rates and ocean surface salinity differ in our model with a well resolved vertical temperature profile in the ice and snow and an explicit brine-pocket parameterization compared to a simulation with Semtner zero-layer thermodynamics. Although these differences are important for the climate of the Arctic, the effects of an ice thickness distribution are more dramatic and extend into the northern North Atlantic. Sensitivity experiments indicate that five ice thickness categories with ~ 50 cm vertical temperature resolution captures the effects of the ice thickness distribution on the heat and freshwater exchange across the surface in the presence of sea ice in climate simulations.

1. Introduction

Climate change simulations with enhanced greenhouse gas scenarios show amplification of surface warming in the polar regions, especially in the Arctic [e.g., *Manabe and Stouffer*, 1980]. And there is evidence for strong interannual and decadal variability in these same regions. For example, satellite images of sea ice extent from the past two decades show the ice has receded at a rate of almost 3% per decade [*Cavalieri et al.*, 1997]. Associated with changes in the ice are interannual and decadal scale variability and a decreasing trend in sea level pressure [*Walsh et al.*, 1996] and surface air temperature [*Rigor*, submitted 1998] in the Arctic. Such trends are not as apparent in the Antarctic. Observations in the high latitude regions continue to be patchy and of short duration, and hence the character of decadal scale variability in the polar regions is not well known, presenting a challenge for the detection of climate change. For these reasons, modeling is an essential tool for understanding polar climate variability and predicting climate change.

To properly simulate high-latitude climate, the boundary conditions of the atmosphere and the coupling between atmosphere and ocean need to be represented ac-

[1]Now at Quaternary Research Center, University of Washington, Seattle.

[2]Now at National Center for Atmospheric Research, Boulder, Colorado

curately in the presence of sea ice. Resolving a distribution of sea ice thickness has important consequences for simulations of the coupled atmosphere-sea ice-ocean system. In the fall and winter, young firstyear ice contributes to rapid growth and high rates of brine rejection compared to the mean ice thickness in a region. According to observations and model studies, ice growth rates in the central Arctic Ocean approximately double when averaged over a distribution of ice thicknesses compared to estimates for 3-m ice alone [*Maykut*, 1982; *Steele and Flato*, 1999]. In addition, air-sea heat exchange is enhanced when thin ice is resolved [*Maykut*, 1982]. In the spring thin ice can melt away, which increases the open water fraction and creates a local ice-albedo feedback within the pack ice [*Curry et al.*, 1995]. Because thin ice is more likely to buckle, raft, and form ridges compared to thick ice, resolving the thickness distribution affects the accuracy of the simulated compressive strength and ultimately feeds back on the ice dynamics.

Recent uncoupled sea ice modeling experiments by *Fichefet and Morales Maqueda* [1997] show that the thermodynamic effect of the ice thickness distribution plays a critical role in the seasonal evolution of the ice pack. In addition, *Fichefet and Morales Maqueda* [1997] and *Holland et al.* [1993] highlight the importance of internal melting in brine pockets in Arctic sea ice. However, sea ice models used previously in global coupled climate studies have neglected the physics associated with the ice thickness distribution and often oversimplify sea ice thermodynamics. In this study, we test the sensitivity of a coupled climate model to the thermodynamic and dynamic effects of an ice thickness distribution model with a well resolved vertical temperature profile in the snow and ice where brine pockets are treated explicitly. Our experiments are performed with a global model that includes a full primitive-equation ocean model, a simple energy-moisture balance atmosphere [*Fanning and Weaver*, 1996], and a dynamic-thermodynamic sea ice model.

Sea ice thickness distribution models have been used for basin-scale studies in the Arctic [*Hibler*, 1980; *Flato and Hibler*, 1995]. In these models the thickness is assumed to be distributed uniformly between each category boundary. Consequently sea ice growth/melt requires a procedure known as advection in thickness-space, and thus the method of resolving the thickness distribution is termed Eulerian. Advection in thickness-space causes diffusion among categories, which can be reduced by resolving many thickness categories. The sea ice thermodynamics in the Eulerian models is relatively simple.

We develop and use a Lagrangian ice thickness distribution model for this study because it more naturally accommodates the resolution of a vertical temperature profile in the ice and snow than an Eulerian model. Our method adjusts the thickness distribution to place resolution where it is needed most by allowing the ice in each category to vary in thickness, as in the numerical model presented in *Thorndike et al.* [1975]. This type of model is referred to as a Lagrangian ice thickness distribution (i.e., Lagrangian in thickness space), and it is free of the diffusion associated with thickness advection in the Eulerian models. The Lagrangian method is desirable for climate simulation if it can be integrated with fewer thickness categories than an Eulerian method. One of our sensitivity experiments tests how many thickness categories are needed with the Lagrangian method to address a question posed by the WCRP [1994, p. 49] ACSYS Numerical Experimentation Group.

Sea ice thermodynamics are characterized by the insulating capacity of sea ice and the storage of latent heat in brine pockets. Our thermodynamics are similar to the model of *Maykut and Untersteiner* [1971] but adhere to strict energy conservation as in *Bitz and Lipscomb* [1999]. *Maykut and Untersteiner* [1971] first demonstrated the effect of latent heat storage in brine pockets in a sea ice model with an explicit brine pocket parameterization. Soon after, *Semtner* [1976] presented a pair of simplified sea ice models. In the three-layer model, the effects of brine pockets were mimicked by storing solar radiation transmitted into the ice in a heat reservoir. In the even simpler zero-layer (or zero-heat capacity) model, Semtner assumes a linear temperature profile in the ice, so there is no storage of sensible heat and brine pockets are neglected altogether. Today most dynamic-thermodynamic sea ice models are based on one of the Semtner models for ice thermodynamics. We explore the sensitivity of the sea ice thermodynamics by comparing an integration with a well resolved vertical temperature profile in the ice and snow where brine pockets are treated explicitly to the much simpler Semtner zero-layer model.

We begin with the definitions of the state variables and basic equations governing their evolution. Later in section 2, we describe the physical processes and parameterizations that are components of these basic equations. In section 3, we show model results and sensitivity experiments. Finally, we conclude the study with a discussion in section 4. Although, the model domain is global, we focus our study on the Arctic because the effects of the ice thickness distribution are most pronounced in the Northern Hemisphere.

2. Model description

The model used in this study is a coupled climate model that is comprised of the Geophysical Fluid Dynamics Laboratory-Modular Ocean Model [*Pacanowski*, 1996], a modified version of the energy-moisture balance atmosphere model of *Fanning and Weaver* [1996], and a dynamic/thermodynamic sea ice model that will be described in greater detail below. Ocean, atmosphere, and sea ice employ the same spherical grid, which has horizontal resolution of 1.8° latitude by 3.6° longitude. The atmosphere model consists of a single vertically-integrated layer, and the ocean model has 19 vertical levels. The model is integrated without flux corrections. Since the original presentation by *Fanning and Weaver* [1996], a parameterization to include the effects of surface orography on precipitation has been added. Additionally, converging meridians at the North Pole have been eliminated by rotating the grid poles 13° with respect to the Earths' poles [*Eby and Holloway*, 1994]. On the model grid, the North Pole is shifted into Greenland (see Fig. 1) and the South Pole remains in Antarctica, although not at the true pole.

The only external forcing on the system is solar radiation at the top of the atmosphere and surface wind stress. Because sea ice motion is dictated by wind stress on a wide range of time scales (at least down to the synoptic scale), the wind stress over sea ice should include daily variability [*Häkkinen and Mellor*, 1992]. Ocean currents in non-eddy resolving ocean models vary on much shorter time scales, so daily varying winds over the ocean are not necessary or (due to time step limitations) desirable. Thus, daily varying wind stress is limited to sea ice in the Northern Hemisphere, which is our region of focus in this study. To avoid transmitting daily fluctuations into the ocean beneath sea ice, which would cause spurious wind stress curl at the ice edge, we let the stress transmitted to the ocean be equal to the climatological component of the wind stress. Wind stress forcing is derived from the National Center for Environmental Prediction reanalysis [*Kalnay et al.*, 1996] for the period 1958-1997. We use the wind stress monthly climatological-mean annual cycle for the entire domain and a daily-varying component derived from daily-varying anomalous geostrophic winds over Northern Hemisphere sea ice. Both components are interpolated using linear splines to arrive at values appropriate for the model time step. The two components are then combined by first converting the climatological wind stress $\boldsymbol{\tau}_a$ to a climatological wind $\mathbf{u}$ from the nonlinear drag law

$$\boldsymbol{\tau}_a = \rho_a C_a |\mathbf{u}|(\mathbf{u}\cos\phi + \mathbf{k}\times\mathbf{u}\sin\phi), \qquad (1)$$

with atmospheric density $\rho_a = 1.25$ kg m^{-3}, the drag coefficient $C_a = 0.001$, and turning angle $\phi = 20°$ ($\mathbf{k}$ is the unit vector normal to the Earth's surface). Next, the climatological wind is added to the daily-varying geostrophic wind, and then the combined wind is converted to a wind stress using Eq. 1.

The model was spun up with climatological monthly mean wind forcing for 1000 years with a two-level sea ice model. Next the model was integrated for 720 years with the daily NCEP wind forcing cycled in 40 year intervals with a 5 category ice thickness distribution. All other integrations were spawned at year 520 from the integration with 5 categories and were integrated for an additional 200 years. The time step of the ocean model is one day and the atmosphere and sea ice models is one-half day, with the exception of the solution to the sea ice momentum, which is solved at one-quarter day time steps.

2.1. Ice model basic equations

Equations governing the evolution of ice and snow velocity, concentration, volume, and energy are developed in this section. Table 1 lists the state variables.

Ice velocity $\mathbf{u}$ is determined from the momentum balance equation,

$$m\frac{D\mathbf{u}}{Dt} = -mf\mathbf{k}\times\mathbf{u} + \boldsymbol{\tau}_a + \boldsymbol{\tau}_w - mg\nabla Y + \nabla\cdot\sigma, \quad (2)$$

where m is the mass per unit area of the ice, f is the Coriolis parameter, $\boldsymbol{\tau}_a$ and $\boldsymbol{\tau}_w$ are forces due to air and water stresses, g is the acceleration due to gravity, Y is the ocean surface dynamic height, and $\nabla\cdot\sigma$ is the force due to internal ice stress. The momentum equation is solved using the elastic-viscous-plastic model of *Hunke and Dukowicz* [1997] with elliptical yield curve aspect ratio, e=2.

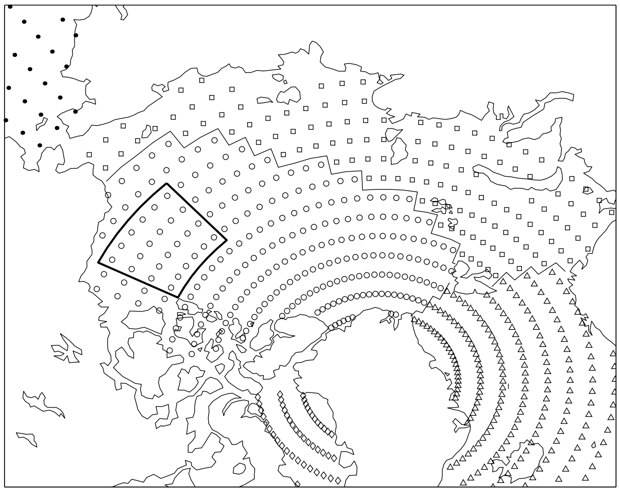

Figure 1. Model grid in Arctic showing converging meridians in Greenland. Symbols are used to define regions where circle=central Arctic, square=shelf region, triangle=Greenland/Norwegian/Iceland (GIN) Seas, and diamond=Labrador Sea/Davis Strait. The enclosed region in the western Arctic is used for averaging below.

In our formulation of the ice-thickness distribution, each category has a single thickness of ice, which is allowed to vary in response to ice growth/melt, advection, and deformation. Our ice thickness distribution model resembles the model of *Thorndike et al.* [1975], who interpolated the thickness distribution to a grid fixed in thickness space at each time step. This method was used in the AIDJEX model [*Coon et al.*, 1974]. Our method has more in common with that shown in *Rothrock* [1986] where the interpolation process was eliminated and each category was allowed to vary freely in thickness for a one-year simulation. However, to maintain a reasonable number of categories in a longer simulation, the number of categories must be limited. We accomplish this by constraining each category to lie between lower and upper thickness limits that are fixed. When a category outgrows its limits, the ice is transfered from one category to another, where it is merged with ice that may already exist by conserving volume, energy, and area. Other techniques for limiting the number of categories have been used by *Björk* [1992] based on merging categories that are closest in thickness. *Schramm et al.* [1997] also defined lower and upper thickness limits, but they allowed more than one category within each pair of thickness limits and merged categories to maintain a roughly constant number within each thickness range. We restrict the number of categories to one within each thickness range to simplify the rules needed for merging.

Although it might be useful for diagnostic purposes to have a separate thickness-distribution for different ice types, in this study the thermodynamic properties are assumed equivalent for firstyear and multiyear ice as well as ridged and level ice, so each category includes all ice types. We prefer not to combine all ridged ice into a single ridged ice category, because observations [*Vinje et al.*, 1998] and models [*Schramm et al.*, 1997] show that ridged ice is broadly distributed and roughly half of the ice in the range of 0-200 cm is ridged. Relatively minor modifications would render the model capable of maintaining separate distributions for different ice types, but the memory requirements and integration time would increase accordingly.

The thickness-distribution, $g(h)$, for M categories is written

$$g(h) = g_0\delta(h) + \sum_{i=1}^{M} g_i\delta(h - H_i) \tag{3}$$

where M is the number of ice categories, $\delta(h)$ is the Dirac delta function, H_i is the thickness, and g_i is the concentration within category i (category 0 is open water). H_i varies in time and is constrained to range between the limits $\hat{H}_{i-1}$ to $\hat{H}_i$ (with $\hat{H}_{-1} = 0$, $\hat{H}_0 =$ 10 cm, ... $\hat{H}_M = \infty$). Although H_i is not a state variable, it may be diagnosed at any time from V_i/g_i.

The evolution of ice concentration and ice volume per unit area, V_i, for each category is governed by a pair of continuity equations,

$$\frac{\partial g_i}{\partial t} = -\nabla \cdot (\mathbf{u}g_i) + \Psi_i + \mathcal{G}_i \tag{4}$$

and

$$\frac{\partial V_i}{\partial t} = -\nabla \cdot (\mathbf{u}V_i) + \Theta_i + \mathcal{V}_i, \tag{5}$$

Table 1. State Variables

symbol	description
$\mathbf{u}$	velocity of the sea ice
g_i	concentration of sea ice in category i
V_i	volume of sea ice in category i
V_i^s	volume of snow in category i
$E_i(z_i^*)$	energy of melting for sea ice[a] in category i

[a] z_i^* is the normalized vertical coordinate in the ice.

respectively, where $\mathbf{u}$ is the velocity of the ice, Ψ_i and Θ_i are contributions by mechanical redistribution, and $\mathcal{G}_i$ and $\mathcal{V}_i$ are contributions by thermodynamic processes. Equation 5 describes the evolution of snow volume when V_i, Θ_i, and $\mathcal{V}_i$ are replaced with V_i^s, Θ_i^s, and $\mathcal{V}_i^s$, respectively.

Employing a vertical coordinate that is normalized by the sea ice thickness, $z_i^* = z/H_i$, the energy of melting, $E_i(z_i^*)$ (i.e., the energy required to melt a unit area of ice, as defined below), evolves according to

$$\frac{\partial E_i}{\partial t} = -\nabla \cdot (\mathbf{u}E_i) + \Pi_i + \mathcal{E}_i, \tag{6}$$

where $\Pi_i(z_i^*)$ is the contribution by mechanical redistribution and $\mathcal{E}_i(z_i^*)$ is the contribution by thermodynamic processes.

The form of equations 4-6 are unique to the the Lagrangian formulation. In our case, because $g(h)$ is comprised of delta functions, the concentration of ice in a given category is unaffected by growth/melt, and the term that contributes to thickness advection in Eulerian models is absent from Eq. 4. Presently, no Eulerian models have need for a continuity equation like Eq. 6 because they do not resolve a vertical temperature profile. If they did, they would require an additional term to describe the advection of energy due to growth/melt. Finally, Eq. 5 is not needed for Eulerian models because the thickness of each category is by definition equal to the midpoint of the category limits.

2.2. Mechanical redistribution and ice strength

We briefly outline our method of evaluating Ψ. Further details that are specific to our Lagrangian formulation of the thickness distribution, including evaluation of Θ_i and Π_i are described in Appendix A. The parameterization of lead opening and mechanical redistribution follows from *Thorndike et al.* [1975]:

$$\Psi = |\dot{\epsilon}|[\alpha_0(\theta)\delta(h) + \alpha_r(\theta)w_r(h,g)], \tag{7}$$

where $|\dot{\epsilon}| = (\dot{\epsilon}_I^2 + \dot{\epsilon}_{II}^2)^{1/2}$, $\dot{\epsilon}_I$ and $\dot{\epsilon}_{II}$ are strain rate invariants, $\theta = \tan^{-1}(\dot{\epsilon}_{II}/\dot{\epsilon}_I)$, and $w_r(h,g)$ is the ridging mode. The coefficients $|\dot{\epsilon}|\alpha_0(\theta)$ and $|\dot{\epsilon}|\alpha_r(\theta)$ are called the lead opening and closing rates, respectively, and they are related by $|\dot{\epsilon}|\alpha_0(\theta) - |\dot{\epsilon}|\alpha_r(\theta) = \dot{\epsilon}_I$. Based on an energetics argument from *Rothrock* [1975] relating $\alpha_r(\theta)$ to the yield curve, *Hibler* [1980] found

$$|\dot{\epsilon}|\alpha_r(\theta) = \frac{1}{2}(\Delta - \dot{\epsilon}_I), \tag{8}$$

where $\Delta = (\dot{\epsilon}_I^2 + \dot{\epsilon}_{II}^2/e^2)^{1/2}$ for the elliptical yield curve. Equation 8 was derived for the viscous-plastic constitutive law and we have neglected extra terms associated with the $\partial\sigma/\partial t$ term in the elastic-viscous-plastic constitutive law.

Flato and Hibler [1995] argued that Eq. 8 can be written as a sum of two terms representing the energy dissipation by shear and convergence:

$$|\dot{\epsilon}|\alpha_r(\theta) = C_s\frac{1}{2}(\Delta - |\dot{\epsilon}_I|) - min(\epsilon_I, 0), \tag{9}$$

with the factor C_s added so the shearing component of mechanical energy dissipation by ridging may be varied (Eq. 8 and Eq. 9 are equivalent when $C_s = 1$). As in *Flato and Hibler* [1995], we let $C_s = 0.5$ unless otherwise noted.

The ridging mode $w_r(h)$ is the sum of two distributions describing the ice participating in ridging $a(h)$ and the ice transformed from ridging $n(h)$, normalized to properly conserve area and volume. The ice participating in ridging comes from weighting $g(h)$ by a function $b(h)$ that is designed to make thinner ice more likely to ridge than thicker ice. *Thorndike et al.* [1975] suggested a plausible $b(h)$ might decrease linearly with the cumulative thickness distribution up to some value G^*. We adopt Thorndike et al.'s postulated $b(h)$ with $G^* = 0.15$. The ice transformed from ridging $n(h)$ is derived from the redistribution process $\gamma(h_1, h_2)dh_2$, which describes the increase in the concentration of ice in the interval $(h_2, h_2 + dh_2)$ when a unit of ice of thickness h_1 ridges. We follow *Hibler* [1980] who constructed a rule, based on observations, that forces all ice participating in ridging to be linearly distributed between ice that is $2h$ and $2\sqrt{Kh}$ where $K = 10^4$ cm.

The ice strength is parameterized using an energetics argument from *Rothrock* [1975] for plastic deformation where the compressive strength is equated with the potential energy increase per unit strain in pure convergence. The potential energy is increased by multiplying by a constant Z to account for the rate of frictional energy loss in ridging,

$$P = Zc_p \int_0^\infty h^2 w_r(h) dh \tag{10}$$

where $c_p = 0.5(\rho/\rho_w)\hat{g}(\rho_w - \rho)$, $\hat{g}$ is the acceleration of gravity, and ρ is the sea ice density. Based on *Hopkins and Hibler* [1991] and *Flato and Hibler* [1995], Z is assumed to be 17.

2.3. Sea ice thermodynamics

In this section we focus on the aspects of the thermodynamics that are unique to the ice-thickness distribution, which include the open water energy balance and new ice growth over open water. We discuss processes that contribute to $\mathcal{G}_i$, $\mathcal{V}_i$, and $\mathcal{E}_i(z_i^*)$, although in practice these terms are eliminated from Eqs. 4–6, and the continuity equations are solved simultaneously with the set of equations that describe the thermodynamic processes that are outlined below.

Vertical temperature profile

Vertical heat conduction and storage in the sea ice are governed by the heat equation. The vertical temperature profile is resolved in the ice in roughly 50-cm intervals, so the number of vertical layers N_i for category i depends on the thickness limits for that category. For example, ice categories with 100 cm and thinner ice have 2 layers and categories with 100-200 cm ice have 4 layers, etc. The maximum number of layers for any category is 8.

Bitz and Lipscomb [1999] developed a method for conserving energy in a model that treats brine pockets explicitly and allows solar radiation to penetrate the top surface of the sea ice. We use the same method to solve the heat equation, to compute top and bottom surface energy balances, and to determine ice growth rates. However, in this study the albedo is a function of ice thickness as in *Ebert and Curry* [1993], and it is computed separately for each category.

Following *Bitz and Lipscomb* [1999], the amount of energy needed to melt a unit volume of sea ice with salinity S at temperature T in Celsius, is equal to

$$q(S,T) = \rho c_o(-\mu S - T) + \rho L_o\left(1 + \frac{\mu S}{T}\right), \tag{11}$$

where c_o and L_o are the heat capacity and latent heat of fusion for fresh ice and μ is the empirical constant from the linear approximation relating the melting temperature and the salinity of sea ice $T_m = -\mu S$. The units of q are J m^{-3}. Thus the energy of melting for layer l in category i in Eq. 6 is

$$E_{i,l} = q(S_{i,l}, T_{i,l})\frac{V_i}{N_i}. \tag{12}$$

In Eqs. 11 and 12, the salinity profile is specified to vary in space but not in time as in *Bitz and Lipscomb* [1999] and *Maykut and Untersteiner* [1971]. The profile, based on observations from *Schwarzacher* [1959], varies from 0‰ at the top to 3.2‰ at the bottom surface, but the ice is assumed fresh for purposes of computing the freshwater exchange with the atmosphere and ocean.

Snow is allowed to accumulate to different depths over each thickness category, and snow is converted into ice when the snow-ice interface is submerged below the ocean surface by the weight of the snow. The snow is assumed fresh and the heat capacity is set equal to zero to be consistent with precipitation in the atmosphere. Thus, $q^s = \rho_s L_o$, where ρ_s is the density of snow. The energy of melting for snow is simply $E_i^s = q^s V_i^s$, which is not consider to be a state variable because it is redundant with the snow volume.

Open water energy balance

Heat transfer between the ocean and ice is partitioned between lateral and bottom melt according to parameterizations that depend on the temperature of the water of the upper ocean layer. The flux of heat into the ocean at the upper surface is

$$F_{net} = g_0 F_0 + \sum_{i=1}^{M} [g_i(I_i - X_{bi}) - X_{ai}] \qquad (13)$$

where F_0 is the net heat flux from the atmosphere into open water (g_0), I_i is the solar radiation passing through the bottom of thickness category i, X_{ai} and X_{bi} are the lateral and bottom heat fluxes into the ice (see fig. 2a). According to Beer's Law, the solar radiation passing through the bottom of thickness category i in Eq. 13 is $I_i = I_0 e^{-H_i \kappa}$ where $I_0 = 0.27$ and $\kappa = 0.015$ cm^{-1}. The net heat flux from the atmosphere into open water is

$$F_0 = F_r(1 - \alpha_0) + F_L - \sigma T_w^4 + F_{so} + F_{eo}, \qquad (14)$$

where T_w is the upper-ocean temperature (here in Kelvin), α_0 is the albedo of the ocean, F_{so} and F_{eo} are the sensible and latent heat fluxes over open water, respectively, F_r is the downward solar radiation, and F_L is the net longwave radiation.

Parameterizations for lateral and bottom heat fluxes into the ice (X_a and X_b in Eq. 13, with the index i implied) depend on the rates the lateral and bottom interfaces are melting, which, in turn, are functions of the ocean surface temperature. Assuming lateral melting occurs uniformly over the interface, the lateral heat flux is

$$X_a = -pHm_1(T_w - T_f)^{m_2} \left(\sum_{l=1}^{N} q_l + q^s \right) \qquad (15)$$

where p is the perimeter of the ice-open water interface, T_f is the freezing temperature of sea water, and m_1 and m_2 are empirical constants. The expression $m_1(T_w - T_f)^{m_2}$ can be thought of as a melt rate. By analyzing ablation data taken during the Marginal Ice Zone Experiment, *Maykut and Perovich* [1987] determined best fit estimates for $m_1 = 3\text{x}10^{-6}$ m s^{-1} deg^{-1} and $m_2 = 1.36$. The bottom heat flux is parameterized according to *McPhee* [1992]:

$$X_b = c_h u_\tau (T_w - T_f) \rho_w c_w, \qquad (16)$$

where $c_w = 4218$ J kg^{-1} deg^{-1} is the heat capacity of water, $c_h = 0.0058$ is an empirical constant, and $u_\tau = 0.02$ m s^{-1} is the skin friction velocity.

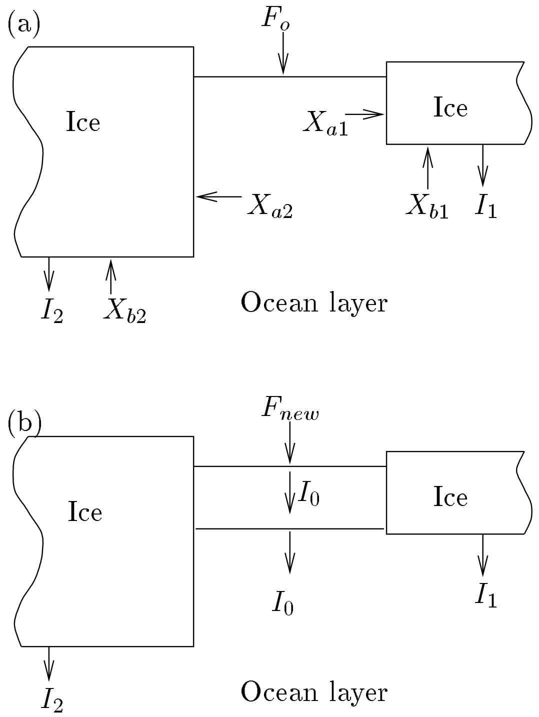

Figure 2. Schematic of open water energy balance for ice free conditions (a) and when new ice is growing (b). Only two categories are shown for simplicity.

The perimeter depends on the floe distribution and geometry. *Rothrock and Thorndike* [1984] developed the concept of a "mean caliper diameter", d, as the average over all angles of the distance between two parallel lines set against the floe's side walls. Thus the interface perimeter is simply $p = n\pi d$, where the number of floes, n, is the ice area divided by the average floe area. Using aerial photographs of summer pack ice in the Beaufort Sea, *Rothrock and Thorndike* [1984] estimated the floe area can be approximated by $0.66d^2$. Following *Steele* [1992], we assume that the floe size can be described by an "average diameter" representing a regional ensemble average. Based on the distribution of the floe diameter in terms of the areal concentration from *Rothrock and Thorndike* [1984], a reasonable estimate for d is 10 km. However, *Steele* [1992] showed that lateral melting is important only for $d < 30m$ in the central Arctic. Because T_w is the temperature of the 25 m upper ocean layer and the lead temperature is not resolved separately, we let $d = 1$ km, independent of ice thickness category.

With this crude estimate, significant lateral melt only occurs in the marginal ice zone where $T_w >> T_f$. However, resolving thin ice with the thickness-distribution model allows thin ice to disappear, so there is a source of open water as thin ice melts away during the melt season. Resolving thin ice eliminates the need for partitioning an unrealistically high fraction of the ocean-ice heat flux towards lateral melt.

New ice growth over open water

New ice grows over open water when the ocean energy balance is such that T_w would fall below the freezing temperature of sea water. When new ice begins to grow, the net heat flux into the ocean is (see Fig.2b)

$$F^*_{net} = g_0(F_0 + I_0)/2 + \sum_{i=1}^{M} g_i I_i, \tag{17}$$

where we average the flux over the open water fraction for conditions with and without new ice present. The solar radiation penetrating the top surface of new ice I_0 is assumed to pass through the ice.

Assuming a linear temperature profile in the new ice, the thickness H_{new} and top surface temperature T_{new} are determined from a pair of coupled equations,

$$\int 0.5(F_0 + F_{new} - I_0)dt - H_{new}q_{new} = 0 \tag{18}$$

and

$$F_{new} - I_0 + \frac{k}{H_{new}}(T_f - T_{new}) = 0, \tag{19}$$

where $0.5(F_0 + F_{new} - I_0)$ is the average flux into the top surface and q_{new} is the energy of melting per unit volume for new ice. The downward net heat flux from the atmosphere to the new ice is

$$F_{new} = F_r(1 - \alpha_{new}) + F_L - \sigma T^4_{new} + F_{si} + F_{ei}, \tag{20}$$

where α_{new} is the albedo, T_{new} is the top-surface temperature (in Kelvin) of the new ice, and F_{si} and F_{ei} are the sensible and latent heat fluxes over new sea ice, respectively.

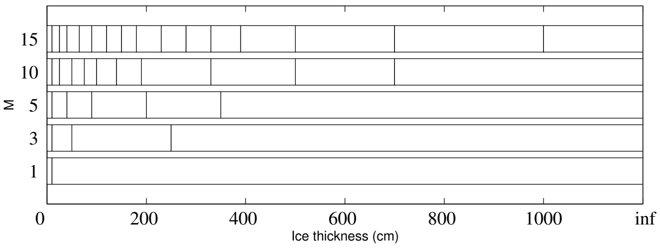

Figure 3. Ice thickness limits for 1, 3, 5, 10, and 15 category integrations. In each case, the 0-10 cm range represents open water and is not counted in the number of ice categories.

2.4. Category transfer

Category transfers are necessary when ice in a given category outgrows its limits. The ice is then moved to a category with appropriate limits, where it is merged with ice that may already exist in that category by conserving volume, energy, and concentration. Any new ice that grows over open water is transferred to the thinnest ice thickness category (category one). Because category one ice is constrained to be at least $\hat{H}_0$ (limits are denoted by $\hat{H}_i$ for $0 \geq i < M$), when $H_{new} < \hat{H}_0$ conservation of concentration is relaxed, so the concentrations of category one increases by just $g_o H_{new}/H_0$. Furthermore if at anytime the thickness of category one should fall bellow its lower limit (i.e., $H_1 < \hat{H}_0$), then we set $H_1 = \hat{H}_0$ and $g_1 = V_1/H_0$. The ice in the thickest category is not limited from above, so there is no upper bound on the ice thickness. Fig 3 illustrates the ice thickness limits for simulations that will be discussed below.

3. Experiments

We demonstrate the sensitivity of the climate to the formulation of our Lagrangian ice thickness distribution model with sophisticated thermodynamics in this section. Unless otherwise stated, averaging is performed from 1968-1987 to avoid the effects of initialization in the first decade and trends in the last.

3.1. Simulation with a well resolved ice thickness distribution

First we discuss an integration with a well resolved thickness distribution using 15 thickness categories in addition to an open water category. We focus our description on the western Arctic (illustrated in 1), but the results generalize for the central Arctic. Figure 4 shows the sources and sinks of ice volume as a function of thickness for the western Arctic. Ice below 150 cm experiences net growth, which is compensated primarily by loss to deformation. Transfer of ice from thinner to thicker categories is also an important sink for ice thinner than 40 cm. Sources and sinks in the 0-10 cm thickness range represent new ice growth over open water, which is transferred immediately into the thinnest ice category. The primary source of ice in the 500 cm and greater thickness range is from deformation. It is noteworthy that even ice in the 150-280 cm range experiences a net sink to deformation, suggesting that the thickness distribution within this range should be well resolved to compute the ridging process accurately (see additional discussion in section 3.2). Although this region of the western Arctic undergoes weak net divergence on the annual mean, some categories have a net source from advection owing to the spatial pattern and the annual march of the ice-thickness distribution in adjacent regions.

The mean annual cycle of the ice thickness distribution in the western Arctic is shown in Fig. 5. Firstyear ice can be seen growing on about day 250 in the 10-40 cm range, transferring to the 40-90 cm range on about day 290, and continuing to transfer up to thicker categories until late winter. Firstyear ice, which is defined to be ice that began growing during the current growth season, is generally thinner than about 200 cm. This

Table 2. Ridged Ice Concentration from Submarine Acoustic Under Ice Profiles

Cruise	Location	Date	Ridged Ice	Source
Gurnard	Beaufort Sea	Apr., 1976	19%	*Wadhams and Horne* [1980]
Nautilus	Canada Basin	Aug., 1958	22%	*McLaren* [1989]
Queenfish	Canada Basin	Aug., 1970	12%	*McLaren* [1989]
Nautilus	Transpolar/Eurasian	Aug., 1958	39%	*McLaren* [1989]
Queenfish	Transpolar/Eurasian	Aug., 1970	27%	*McLaren* [1989]
Sovereign	North of Greenland	Oct., 1976	40-46%	*Wadhams* [1986]
British	North of Greenland	May, 1987	31-45%	*Wadhams* [1990]
British	Fram Strait	May, 1987	65%	*Wadhams* [1992]

thickness is also the cutoff for ice that experiences net growth or net melt (see Fig. 4). The concentration of ridged and multiyear ice is on average 80%, leaving 20% split between firstyear ice and open water.

Fig. 5 shows that the concentration of ice thicker than 500 cm is about 40% year round in the western Arctic. Estimates of the observed ridged ice (typically defined as ice thicker than 500 cm) concentration in the Beaufort Sea and Canada Basin range from 19-22% from submarine cruises (see Table 2). Observed ridged ice concentrations is 31–65% in regions north of Greenland and in Fram Strait, where the model concentration of ice thicker than 500 cm is still about 40% on average (not shown). While the agreement in the eastern Arctic is reasonable, the model appears to ridge too easily and/or cannot melt thick ice fast enough in the western Arctic. A sensitivity study comparing ice model formulations for the elliptical yield rheology by *Arbetter et al.* [1999] indicates that the elastic-viscous-plastic model produces nearly the same fraction of ridged ice-covered area as the viscous-plastic formulation of *Zhang and Hibler* [1997]. Thus we reject the possibility that elastic waves are causing too much ridging. While it is discouraging that the thickness distribution model produces too much thick ice in the western Arctic, we will see below that the climate system response differs little when the ice model is tuned to produce less ridged ice

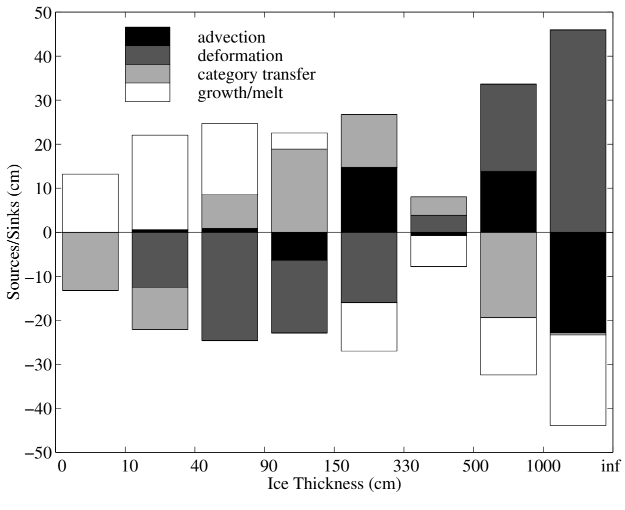

Figure 4. Annual volume balance for ice in the western Arctic (boxed region in Fig. 1). Net sources and sinks are shown averaged over the region (e.g., ice growth in the 10-40 cm range is a source of 23 cm of ice per unit area per year). Ice growth/melt is summed over the top, bottom, and lateral surfaces. The 15 categories are combined into 8 thickness partitions to simplify visualization.

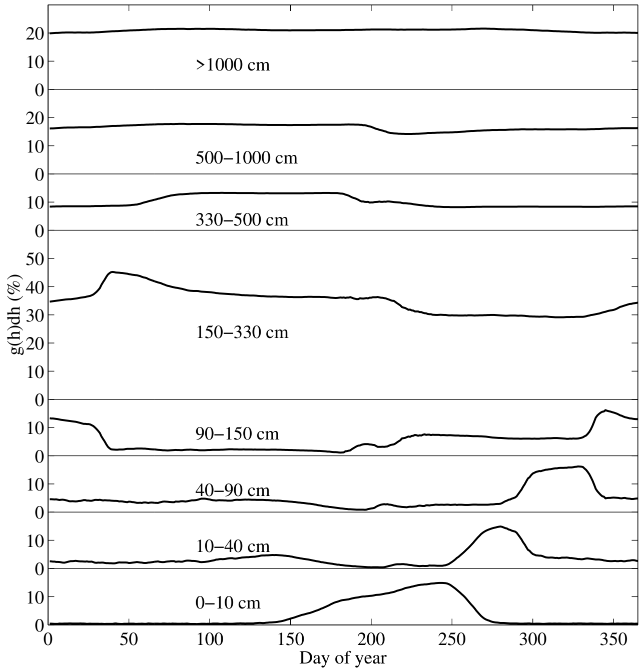

Figure 5. Mean annual cycle of g(h)dh in the western Arctic (see box in Fig. 1). As in Fig. 4, the 15 categories are combined into 8 partitions. Vertical-axis ticks denote 20% concentration increments.

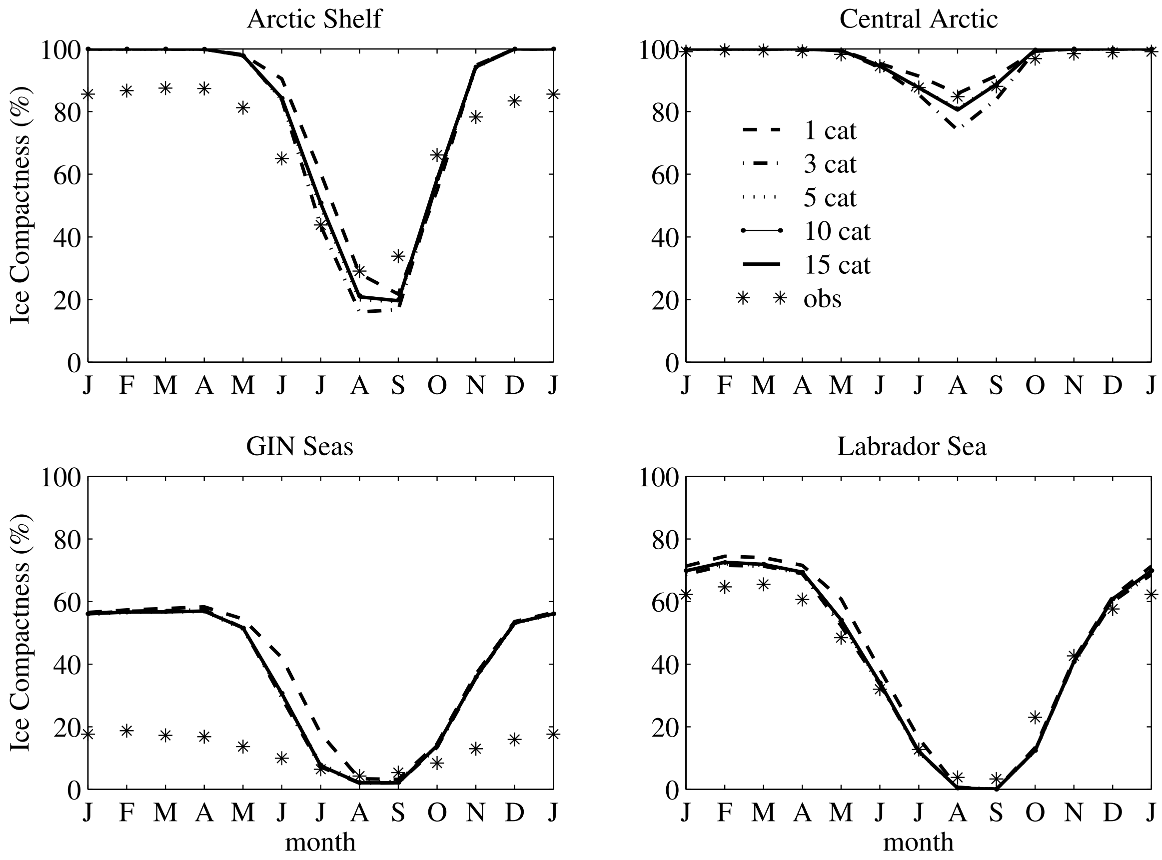

Figure 6. Mean annual cycle of ice compactness for 1, 3, 5, 10, and 15 category integrations separated into subregions defined in Fig. 1. Stars denote observed ice compactness from the Walsh data set [*Chapman and Walsh*, 1993]. The curves for the 5-15 category cases are often indistinguishable.

there (see section 3.6).

The need to resolve ice thinner than 100 cm has long been recognized as important because the thermodynamics are a strong function of thickness for thin ice [e.g., *Maykut*, 1982; *Schramm et al.*, 1997]. However, it is perhaps equally important to resolve thin ice when computing the compressive strength for dynamical processes. There is a period from about day 45–165 when the thinnest 15% of the ice thickness distribution includes ice thicker than 150 cm. Fig. 4 indicates that about 1/4 of the ice that deforms comes from ice thicker than 150 cm and nearly 1/2 comes from ice thicker than 90 cm. This is consistent with observations near Prudhoe Bay Alaska, where half of the ridges measured were formed from ice blocks in excess of 100 cm [*Tucker and Govoni*, 1981]. Thus, it is important to resolve the distribution of ice in the range $100 - 200$ cm to properly compute the ice mechanical redistribution and compressive strength.

The spatial pattern of ice thickness and other relevant quantities are given in section 3.3, where they are shown side-by-side with an integration without an ice thickness distribution model. For now we digress to address the question, how many ice categories are necessary in a coupled model?

3.2. Sensitivity to number of ice categories

Differences between integrations with $M = 1$, 3, 5, 10, and 15 ice thickness categories are explored in this section (see Fig. 3 for a schematic of the category thickness limits). Each case also has an open water fraction, which is not counted in M. Hence, our one category model is similar to what is more commonly called a "two-level" model. We prefer not to use the word level to describe categories because it tends to be easily confused with layers, which we use exclusively for the vertical grid. Ice compactness, thickness, growth rates, and compressive strength will be used to diagnose differences between integrations. Our focus on the mean annual cycle isolates processes by season.

In each case, all parameters are held fixed except for the number of categories. Because the compressive

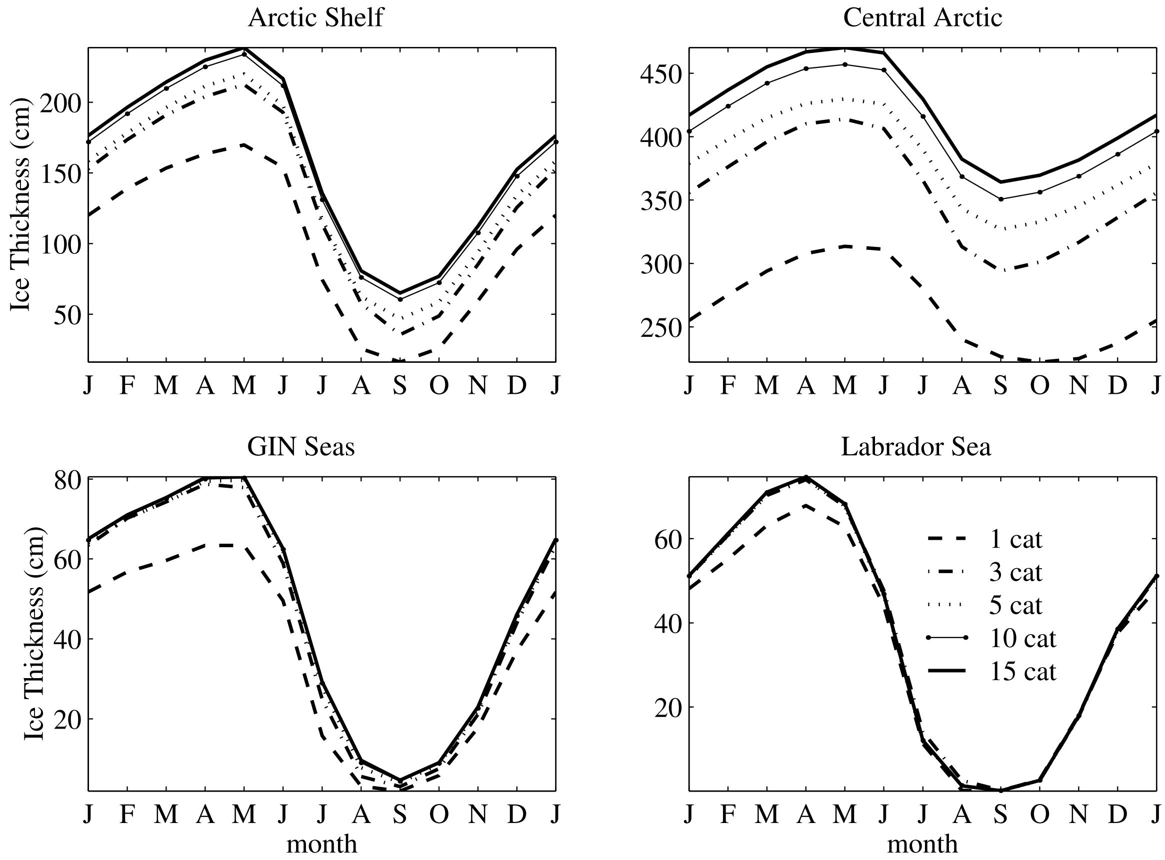

Figure 7. As in Fig. 6 but for ice thickness.

strength computed by Eq. 10 depends on g(h), we use an empirical formula for cases when g(h) is not resolved adequately (i.e., $M \leq 3$), based on the formula *Hibler* [1979] used for the two-level model:

$$P = P^* \sum_{i=1}^{M} V_i e^{-Cg_0}, \tag{21}$$

where $P^* = 27.5$ N/m^2 and $C = 25$. Lead opening and closing rates are computed from the same expression, independent of the number of categories. As suggested by *Stern et al.* [1995], we make a modification to the traditional two-level model of *Hibler* [1979] to allow shearing deformation to contribute to opening and closing of leads when $M = 1$.

Figures 6 and 7 show the mean annual cycle of ice compactness, $\sum_{i=1}^{M} g_i$, and thickness, $\sum_{i=1}^{M} V_i$, as a function of the number of categories resolved in the integration. The curves are separated into four subregions that are identified in Fig. 1. Although the multi-category integrations have substantially thicker ice, the compactness of ice is greatest for the one-category integration in all regions. Because the lead opening rate is computed independent of M, the multi-category integrations can only have more open water than the one-category integration if (1) the ice compressive strength is lower or (2) thin ice categories melt away completely. The mean annual cycle of ice strength within the Arctic Basin (not shown) during winter and the onset of the melt season, allows us to discard hypothesis (1) because the multi-category integrations have higher compressive strength. The compressive strength is near zero for all integrations in all regions by mid June. Thus melting away of thin ice categories is the primary reason for lower compactness in the multi-category integrations compared to the one-category integration.

The mean annual cycle of ice compactness converges in all four subregions for integrations with five or more categories and in the subpolar seas for integrations with as few as three. Curiously, the ice compactness in the three category integration does not lie between the one- and 15-category integrations in the Arctic Basin. With 3 categories the ice is much thinner than cases with more categories, which causes the thin ice categories to disappear earlier in the melt season and enhances the local ice-albedo feedbacks in the pack. Although it is difficult to see in Fig. 6, the ice compactness asymptot-

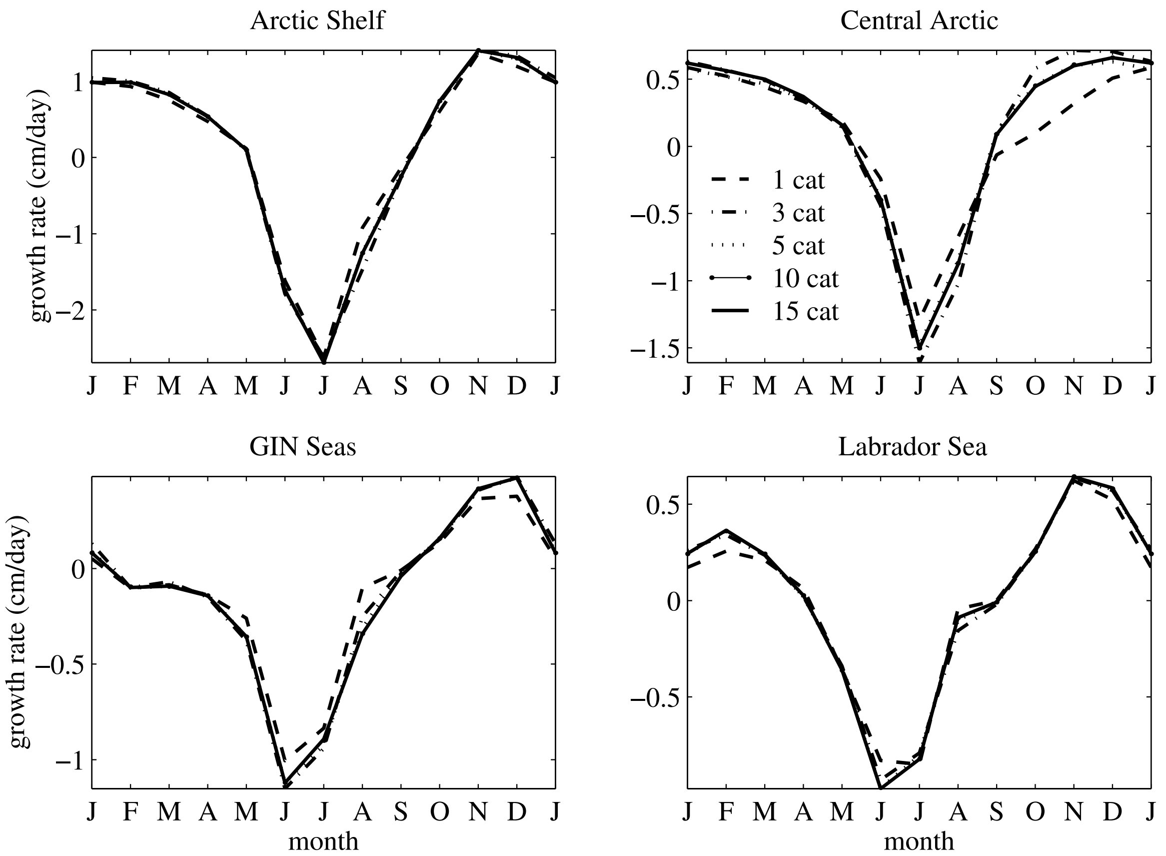

Figure 8. As in Fig. 6 but for ice growth rates.

ically approaches that of the 15-category simulation for $M \geq 3$.

The simulated compactness compares well with observations all year in the central Arctic and Labrador Sea and for summer in the GIN Seas. Including at least 5 categories improves the simulation at the beginning of the melt season. The most noticeable deviations from observations are in the GIN Seas and arctic shelf, where the ice is too extensive in winter. Typical of course resolution ocean model, North Atlantic deep water forms too far south in our model, and the North Atlantic current does not bring adequate heat into the GIN Seas. As such, we get too much winter sea ice in the northern North Atlantic. Additionally, poor resolution of small-scale shelf-ocean interactions may lead to the abundance of ice in winter along the Siberian shelf. Including a thickness distribution in the ice model cannot make up for such deficiencies in the ocean model.

The mean annual cycle of ice thickness shown in Fig. 7, indicates that thickness converges more slowly as a function of category in the Arctic Basin. The reason for the slow convergence stems from the parameterization for the ice compressive strength (see section 2.2), which depends on the distribution of thin ice within a grid box. For a given g(h), the model estimate of the compressive strength tends to decrease as the thinnest ice is better resolved. Resolving more categories allows the ice to ridge more easily, which leads to more open water, higher growth rates, and thicker ice in the central Arctic. In our model, the ice is overall about 10% thicker with 15 categories compared to 5, yet the compressive strength is only 5% higher.

More rapid convergence could perhaps be reached by tuning $b(h)$ (see section 2.2) so the compressive strength is less sensitive to M. However, our objective was to examine the coupled model response to the number of categories using parameterizations that are already well tested in uncoupled simulations. Because the region where the rate of convergence for the ice thickness as a function of category is slowest in the Beaufort Gyre and East Siberian Seas, another possibility is the model simply builds ridges too easily under shear. The sensitivity of the model to energy dissipation by shear deformation will be discussed further in section 3.6.

Figure 8 shows the mean annual cycle of ice growth rate as a function of number of thickness categories

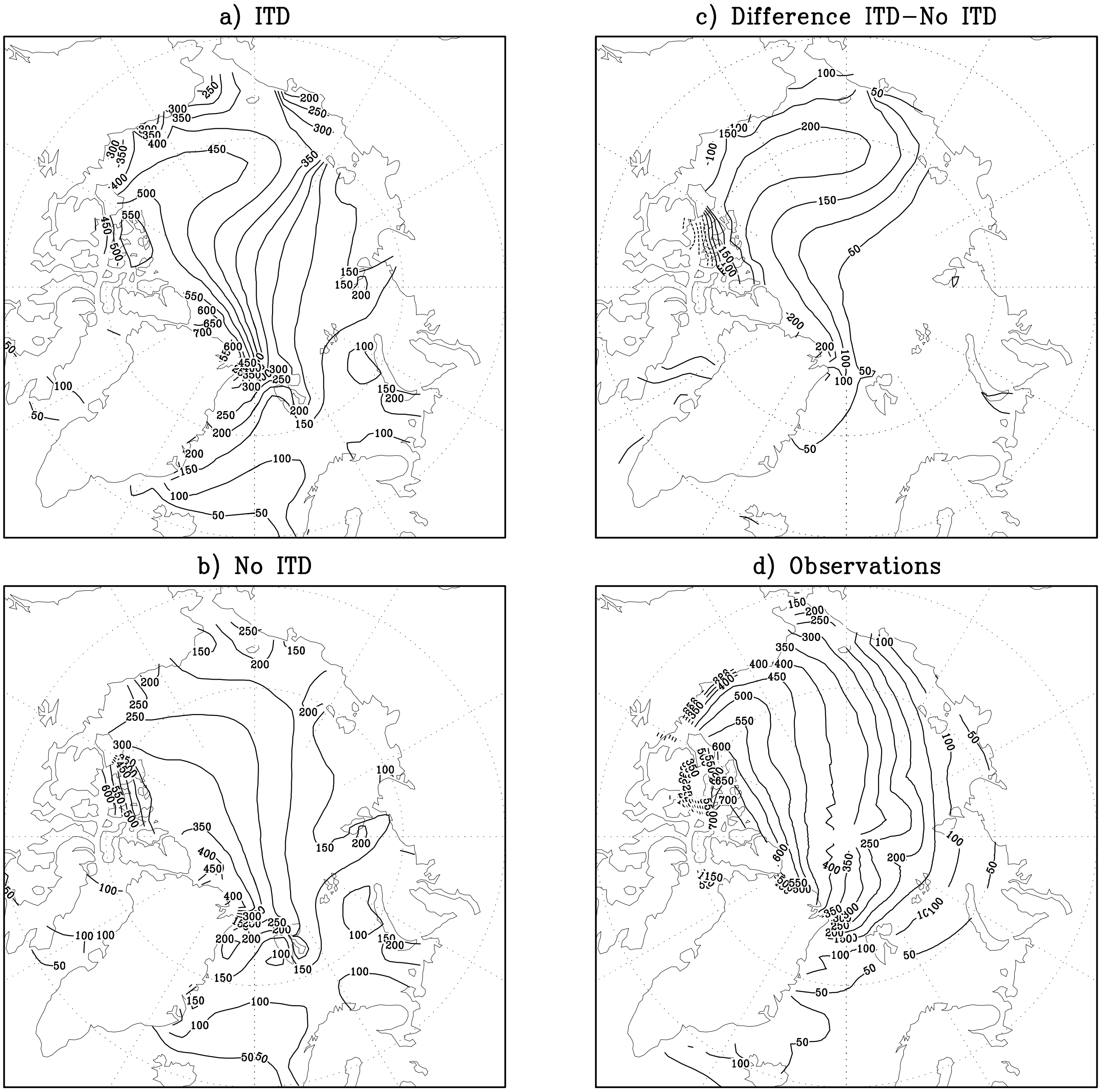

Figure 9. Winter sea ice thickness simulated by the model with (a) and without (b) an ice thickness distribution and their difference (c) and observed winter ice draft (d) from submarine data [*Bourke and Garrett*, 1987]. Contour interval is 50 cm. Winter is defined as Jan.-Mar.

for the subregions. The most substantial differences are seen in the central Arctic in fall when the multi-category integrations resolve thin ice growth well beyond freeze up. Despite the somewhat slow convergence for ice thickness in the Arctic Basin, growth rates for multi-category integration with five or more categories are insensitive to the number of categories. Compared to the multi-category cases, the simulation with a single ice category generally has lower growth rates in every season, which is consistent with a smaller thickness range for the annual cycle shown in Fig. 7. These differences in growth have considerable implications for the fresh water balance and ocean response as will be shown in the following section.

In summary, we found that the seasonal cycle of variables shown in Figs. 6-8 generally indicates that there are substantial differences between the case with just one category compared to those with multiple-categories. Further, our results show diminishing returns for integrations with more than five categories, with the exception of our estimates for ice thickness in the Arctic Basin. However, heat and freshwater exchange with the atmosphere and ocean depends mainly on the concentration of open water and thin ice, which is relatively insensitive to the number of categories beyond $M = 5$. The ice thickness differs with M owing to the distribution of thick ridged ice, but thick ice has only a modest effect on variables that are relevant for coupled climate modeling. From these tests we conclude that just five categories are necessary for properly resolving the seasonal cycle of climatically important variables. However, we caution that the way the categories are defined can affect this conclusion, because it is important to adequately resolve ice below 200 cm thick. A simulation with 5 categories is a reasonable computation expenditure for climate simulations: A time step through thermodynamics, mechanical redistribution, and advection for 5 categories require about 1/2 of the cpu time that is needed for a step through the elastic-viscous-plastic solution of the ice momentum equation. Furthermore, the solution of the momentum equation is often time stepped more frequently than the thermodynamics, mechanical redistribution, and advection (e.g., twice as often in our integrations), so the cost of multiple categories is a small fraction of the total cpu time used by the sea ice model.

3.3. Simulations with and without an ice thickness distribution

In this section, we compare the coupled model response to cases with and without an ice thickness distribution (ITD) by presenting fields of ice thickness and compactness, net freezing rate, latent and sensible heat flux, and ocean salinity. We show results for the thickness distribution using the 5 category simulation based on results from the previous section. The case with no-ITD has just one ice category and one category for open water.

Figure 9a-c shows the winter pattern of sea ice thickness in the Arctic for cases with and without an ITD as well as the difference (ITD-no ITD). For comparison, the observed winter ice draft from submarine cruises [see *Bourke and Garrett*, 1987] is shown in Fig 9d. These data are composed mainly from six submarine tracks taken between 1960 and 1976 and aircraft laser measurements, so the data should be viewed as a collage of snapshots and not a longterm mean. Because none of the cruises sampled the ice in the Siberian Shelf, the comparison of observations and model is most meaningful in the central Arctic.

First comparing model and observations within the Arctic Basin, we see that the case with an ITD compares more favorably in the central Arctic, and the case with no-ITD compares more favorably along the shelf. The ice is 100-200 cm too thick in the East Siberian Sea with an ITD, and 100-200 cm too thin in the central Arctic with no-ITD. The main reason the thickness compares more favorably in the central Arctic for the ITD model is because of the large fraction of ridged ice ($H \geq 500$ cm) in these regions.

Owing to weak heat transport by the ocean and atmosphere, both cases have too much ice in the Greenland, Iceland, and Norwegian (GIN) Seas by about the same magnitude. The GIN Seas are ice free during summer in the model, so the problem is primarily a winter phenomena. Over production of ice in the GIN Seas is typical of coupled atmosphere-sea ice-ocean models that do not employ flux corrections. Perhaps this problem could be eliminated by improved parameterizations of flow over sills and shelf-ocean interactions.

Ice compactness in the ITD case is 10–30% lower in the marginal ice zones and about 2.5% lower in the central Arctic in summer (see Fig. 10). Additionally, the extent is reduced in winter by a few degrees of latitude (not shown). This occurs because thin ice categories disappear quickly in the summer, creating more open water in the case with the ITD. With a larger open water fraction, the upper ocean stores more heat from absorbed solar radiation and retards freeze up longer in the fall. Changes in compactness in the Laptev and Chukchi Seas are as much as 10% higher in Fig. 10, because the ice in the ITD case is much thicker than the no-ITD case and it takes longer to melt back during the summer regardless of positive feedbacks associated with resolving thin ice categories. Also thicker ice is advected into these regions in the case with an ITD.

Figure 11a shows the difference of late winter–spring mean latent plus sensible heat flux at the surface for cases with and without an ITD. To a large extent, the heat flux difference reflects the ice compactness difference pattern in Fig. 10c. The heat flux for the ITD case is 5–15 W m^{-2} higher than the no ITD case over the

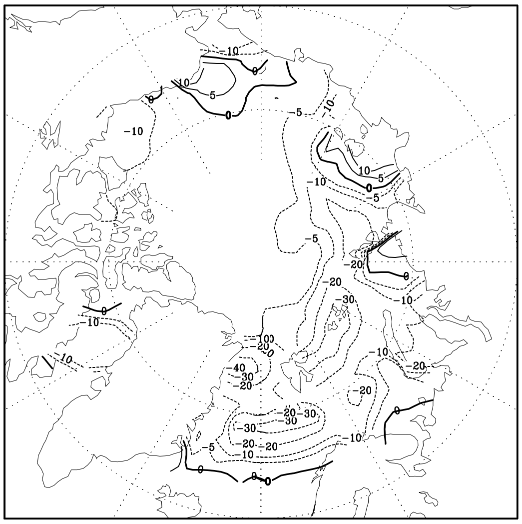

Figure 10. Difference of summer sea ice compactness with and without an ice thickness distribution. Contour interval is 2.5% between +/- 5% and 10% otherwise. Summer is defined as Jul.-Sep.

central Arctic and GIN Seas. The differences amount to about 10–25% of the total in these regions, as typical values for the heat flux in the central Arctic and GIN Seas are approximately 20 W m^{-2}. Even larger differences are associated with changes in the sea ice extent in the Iceland Sea, because the total heat flux south of the ice edge is much greater than that over ice. Ultimately these differences lead to warmer late winter–spring temperatures above the subpolar oceans in the ITD model by about 1° C (see Fig. 11b).

Another important aspect of the ITD model in the Arctic stems from the effect thin ice has on sea ice growth rates. Figure 12d-f shows net freezing rate (NFR), defined as the annual total growth minus melt, after *Steele and Flato* [1999]. We also show growth rates for October (Fig. 12a-c), when growth rate differences with and without an ITD are largest (see Fig. 8). Throughout much of the central Arctic, the October growth rates are more than double in the ITD case compared to the case with no ITD. The NFR differences are only slightly less dramatic, as each year the ITD model grows up to 50 cm more in the central Arctic. To compensate for these differences in growth rate, ice export from the Arctic Basin is about 25% higher for the case with an ITD (see table 3).

In response to increased NFR, the upper ocean salinity is about 0.1‰ higher throughout most of the central Arctic and GIN Seas for the ITD case (see Fig 13). Although increased ice export rates provides a source of freshwater in the GIN Seas, the added freshening is more than compensated by increased transport of higher salinity ocean surface water, due to higher NFR in the central Arctic. Strong negative salinity differences are seen in the east Siberian shelf, owing to the advection of Beaufort Sea ice, which is much thicker in the case with an ITD. This thick ice is a source of freshwater during the summer months, and yet it grows relatively slowly during winter.

3.4. Sea ice interannual variability and its influence on the ocean

It has been postulated that sea ice affects deep water formation in the northern North Atlantic [e.g., *Aagaard and Carmack*, 1989]. Recent modeling studies show that sea ice export is correlated with the thermohaline circulation of the Atlantic [*Holland et al.*, submitted 1999]. We test the sensitivity of the ocean variability

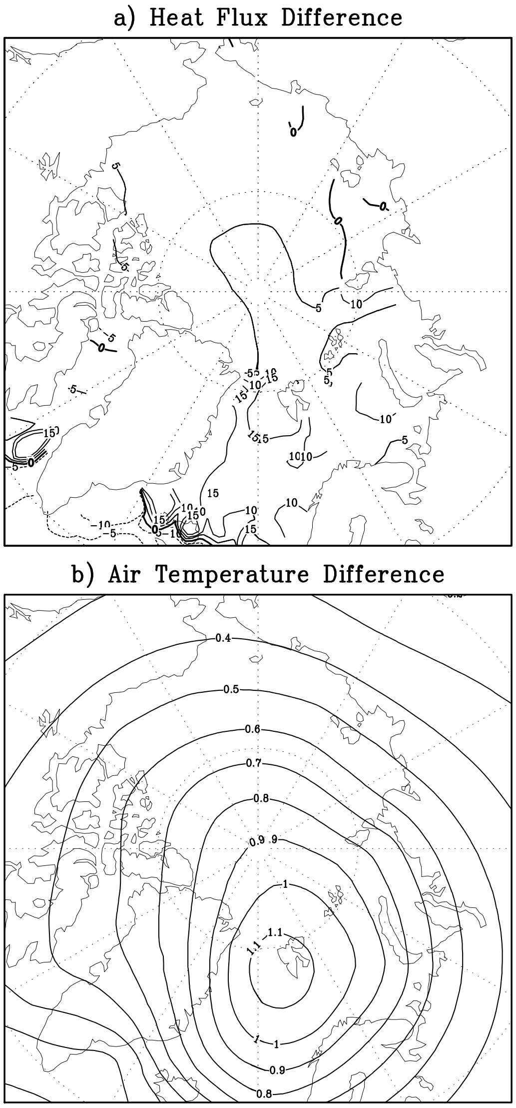

Figure 11. Difference of late winter–spring (Mar.-Jun.) mean latent plus sensible heat flux (a) and surface air temperature (b) with and without an ice thickness distribution. Contour interval is 5 W m^{-2} (up to +/-15 W m^{-2} maximum) for (a) and 0.1° C for (b).

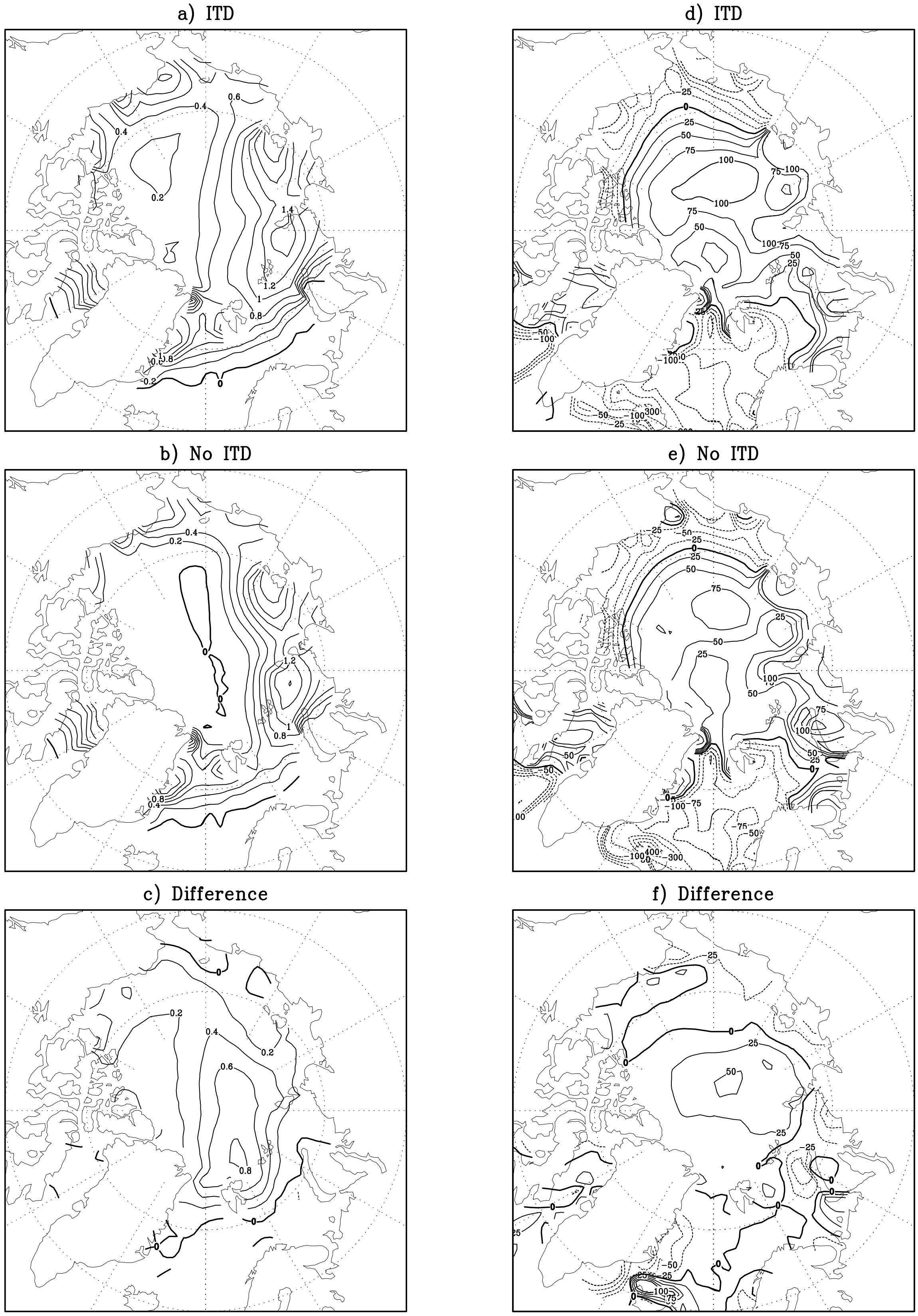

Figure 12. Mean October growth rates (a-c) and annual mean net freezing rates (d-f) with and without an ice thickness distribution and their difference. Units for the left column are cm day^{-1} and for the right column are cm yr^{-1}.

Table 3. Statistics for Time Series in Fig. 14 for Years 1968-1997

variable	mean		standard deviation	
	ITD	No ITD	ITD	No ITD
Volume Flux (km^3 yr^{-1})	2400	1900	640	460
Compactness (%)	36	38	1.5	1.4
Thickness (cm)	48	37	7.5	4.3
Overturning (Sv)	22.9	22.8	.32	.22

Sv = 10^6 m^3 s^{-1}

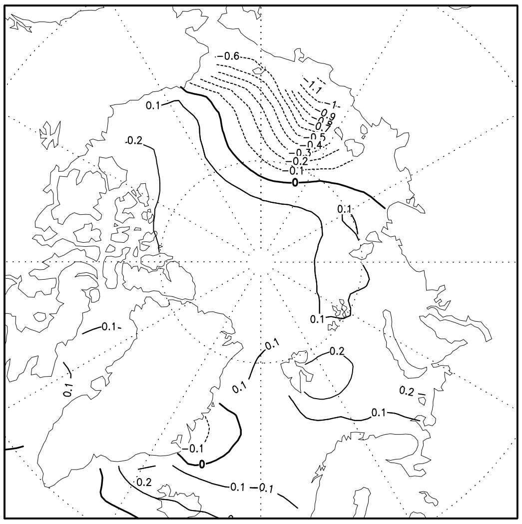

Figure 13. Annual mean salinity of upper 25 m ocean layer difference with and without an ice thickness distribution.

to the formulation of the sea ice physics using the final 40 year cycle of our simulations.

Figure 14 shows time series of the simulated ice export, ice compactness and thickness in the GIN Seas, and the meridional overturning index (defined as the maximum amplitude of the overturning stream function below 200-m depth and north of 40° latitude) for 1958-1997. Observed Fram Strait ice export and GIN Seas ice compactness are also given in Fig. 14. The correlation between observed and modeled ice export anomalies is remarkably high (r=0.91 for either case with and without and ITD), although the modeled time series is a volume flux and the observed is an area flux. The correlations between observed and modeled GIN Seas ice compactness is much less (r=0.42 for the ITD case and r=0.33 for the no-ITD case). Furthermore the amplitude of the observed anomalies are smaller.

A decreasing trend of -2.4% per decade is evident in the last 36 years of the observed ice compactness, while the model trend from 1959-1994 is almost negligible. It is not surprising that the model lacks the observed trend because no anthropogenic forcing is present in the model except through the prescribed wind anomalies, which are not used to advect heat and moisture in the simple energy-moisture balance atmosphere model. Yet, a strong trend in the last decade of the simulation seems to be present among all the variables shown in Fig. 14. The simulated ice export is highly correlated with the North Atlantic Oscillation (NAO) over the second half of the 40 year period, as is seen for the observed ice export [*Kwok and Rothrock*, 1999]. The trend in the NAO is well documented [e.g., see *Hurrell*, 1995]. It is interesting to see that in the absence of prescribed surface warming, the model tends to have an increasing trend in compactness that appears to be related to the NAO.

Sea ice variability and its influence on the ocean meridional overturning stream function depend on the ice thickness distribution, with variability generally higher for the case with an ITD (see table 3). The increased variability for ice export and thickness for the case with an ITD compared to that without may simply reflect higher amplitudes in these quantities. The ocean tends to integrate the freshwater transport and insulating effects of the ice in such a way as to maintain roughly the same overturning amplitude for both cases, but the standard deviation for the case with an ITD is almost 50% greater than the case without an ITD. The most noticeable difference in the overturning occurs from 1989-1997 when the overturning anomaly for the case with an ITD is nearly double the anomaly in the case without one.

Ice thickness and area in the GIN Seas are well correlated with the export for both cases. However, the overturning is only significantly correlated with the sea ice variables in the case with an ITD ($r \sim -0.45$ at 2–4 yr lag). The ice thickness and area tend to increase in response to positive export anomalies, which in turn leads to a decrease in the overturning 2-4 years later. The anomalies are larger in the case with the ITD so the overturning tends to respond more directly to the

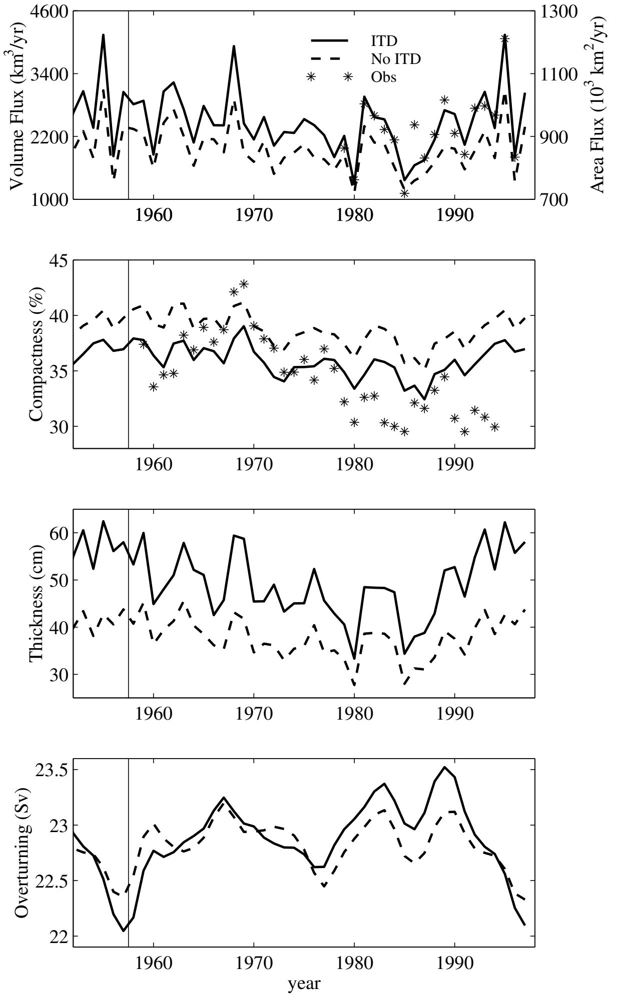

Figure 14. Ice volume flux through Fram Strait, compactness and thickness in the GIN Seas, and meridional overturning index for simulations with and without an ice thickness distribution. Left of the vertical line are the last 5 years of the previous cycle to demonstrate that the model is in equilibrium. Stars denote satellite derived observations of the ice area flux through Fram Strait [*Kwok and Rothrock*, 1999] and ice compactness in the GIN Seas [*Chapman and Walsh*, 1993], which is increased by a constant offset of 22%.

ice and is less likely to be influenced by other factors.

3.5. Sensitivity to storage of latent and sensible heat

Part of the motivation for using a Lagrangian type of ice thickness distribution model is that it more easily accommodates our sophisticated thermodynamics scheme. The multi-layer model includes a vertical temperature profile with a brine pocket parameterization that explicitly allows internal melting in the ice interior. In this section, we compare a simulation with our standard multi-layer (ML) thermodynamics to a case with *Semtner* [1976] zero-layer (ZL) thermodynamics. For simplicity, both cases have a single ice category.

Figure 15 shows the mean annual cycle of ice thickness for ML and ZL cases. The ML case ice is generally thinner in all regions during winter compared to the ZL case. The most striking difference in thickness is in the central Arctic during summer where the ZL case is about 40 cm thinner on average. This thickness difference has the potential of being important in a climate change scenario because positive ice-albedo feedbacks are likely to be stronger in the thin ice case.

The compactness curves that are analogous to Fig. 15 are negligibly different (not shown). Because latent and sensible heat fluxes are sensitive to thin ice and open water area, the insignificant changes in thickness in the marginal seas and compactness throughout the Arctic result in negligible changes to the turbulent heat fluxes. In addition, the surface albedo changes only slightly, so solar radiation also changes very little. These small changes in atmosphere-ice heat exchange cause only minor changes in the surface air temperature.

While the atmosphere changes very little as a result of sea ice thermodynamics, the mean annual cycle of growth rates is very sensitivity to the model differences (see Fig. 16). In the ML case compared to the ZL case, the ice melts (grows) later and at a slower rate in summer (winter). The net effect of ML thermodynamics on the upper ocean layer is to increase the salinity in the central Arctic (see Fig. 17), because melt rate differences in the summer dominate over the wintertime effects. The opposite is true in the southern Beaufort, Chukchi, Kara, and Barents Seas. The greatest differences lie within the Arctic Basin, and these differences are even larger than the salinity difference for cases with and without the ITD. On the other hand, ice export through Fram Strait is nearly unchanged as is the thickness and compactness in the GIN Seas, so deep water formation in the northern North Atlantic changes very little.

Sea ice only model studies of the sensitivity to multilayer thermodynamics by *Fichefet and Morales Maqueda* [1997] and *Holland et al.* [1993] concluded that ice model thermodynamics has a substantial impact on the sea ice cover. Both of these uncoupled studies found the ice was overall thicker and more extensive with Semtner three-layer (3L) thermodynamics compared to zero-layer thermodynamics. It is not clear if our results differ from these studies because our model is coupled or because the 3L thermodynamics differ substantially from our ML thermodynamics. One possibly important model difference concerns solar radiation absorption in the ice. In the 3L model, all solar radiation that penetrates the top surface of the ice contributes to the brine reservoir, which is used to retard cooling in the fall. While in our ML model, solar radiation is absorbed in each layer according to Beer's Law, and some solar radiation passes through the bottom surface of the ice.

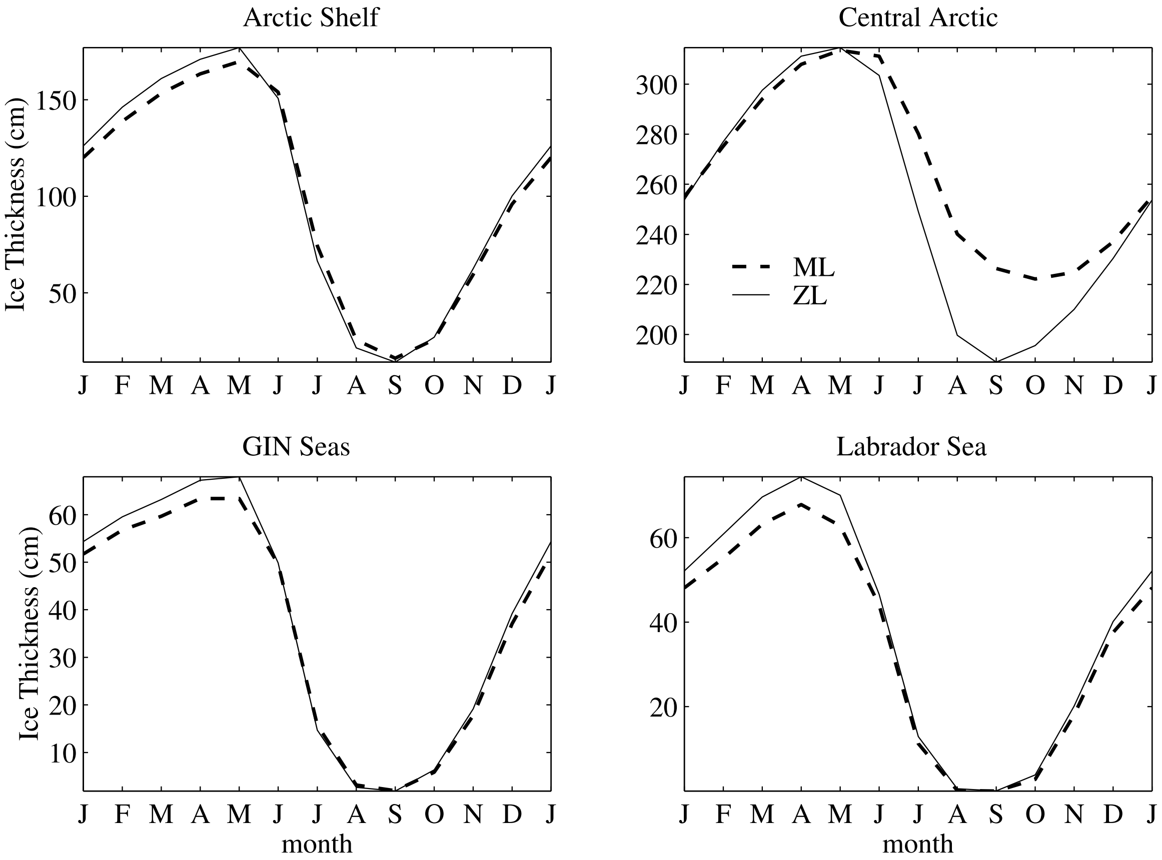

Figure 15. Mean annual cycle of ice thickness for cases with multi-layer (ML) and zero-layer (ZL) thermodynamics separated into subregions defined in Fig. 1.

These model differences are likely to be most apparent in regions with seasonal ice. Furthermore unlike the 3L model our explicit brine pocket parameterization retards warming in the spring.

3.6. Sensitivity to shear deformation

We describe one final experiment that is designed to address the problem identified in section 3.1-3.3 concerning too much thick ridged ice in the Beaufort Gyre in the multi-category simulations. The strong shear in the Beaufort Gyre lends suspicion to the parameterization for ridge building under shear. A fundamental assumption used in the thickness distribution model is that shearing deformation builds ridges using the same functional dependence on g(h) to determine how the ice is broken and piled into ridges [*Thorndike et al.*, 1975]. However, the way shearing deformation contributes to lead opening and closing rates is still a matter of some controversy. Synthetic aperture radar (SAR) images analyzed by [*Stern et al.*, 1995] appear to confirm that shearing contributes an amount that is in good agreement with the elliptical yield curve with e=2 when all energy dissipation by shearing is assumed to build ridges ($C_s = 1$ in Eq. 9). Further evidence suggests that SAR data might only yield an upper limit on the contribution to lead opening from shearing (personal communication, H. Stern and R. Moritz). Nonetheless, comparing the modeled ridged ice thickness distribution with observations lead *Flato and Hibler* [1995] to conclude that a better approximation would apply only half of the energy dissipation by shearing to build ridges ($C_s = 0.5$) with the rest lost to sliding.

We test the sensitivity of the model to shear deformation by comparing our control simulation ($C_s = 0.5$) to a simulation where we neglect deformation from shearing altogether ($C_s = 0$). In both cases, five categories are used. In the limit that the elastic waves are negligibly small, the stress states still lie on or inside the elliptical yield curve with e=2, and the model still properly dissipates energy. However, all of the mechanical energy dissipated by shear is assumed lost to sliding when $C_s = 0$.

The large-scale shape of the thickness pattern in Fig. 18a looks more like the case with no ITD in 9b, excep-

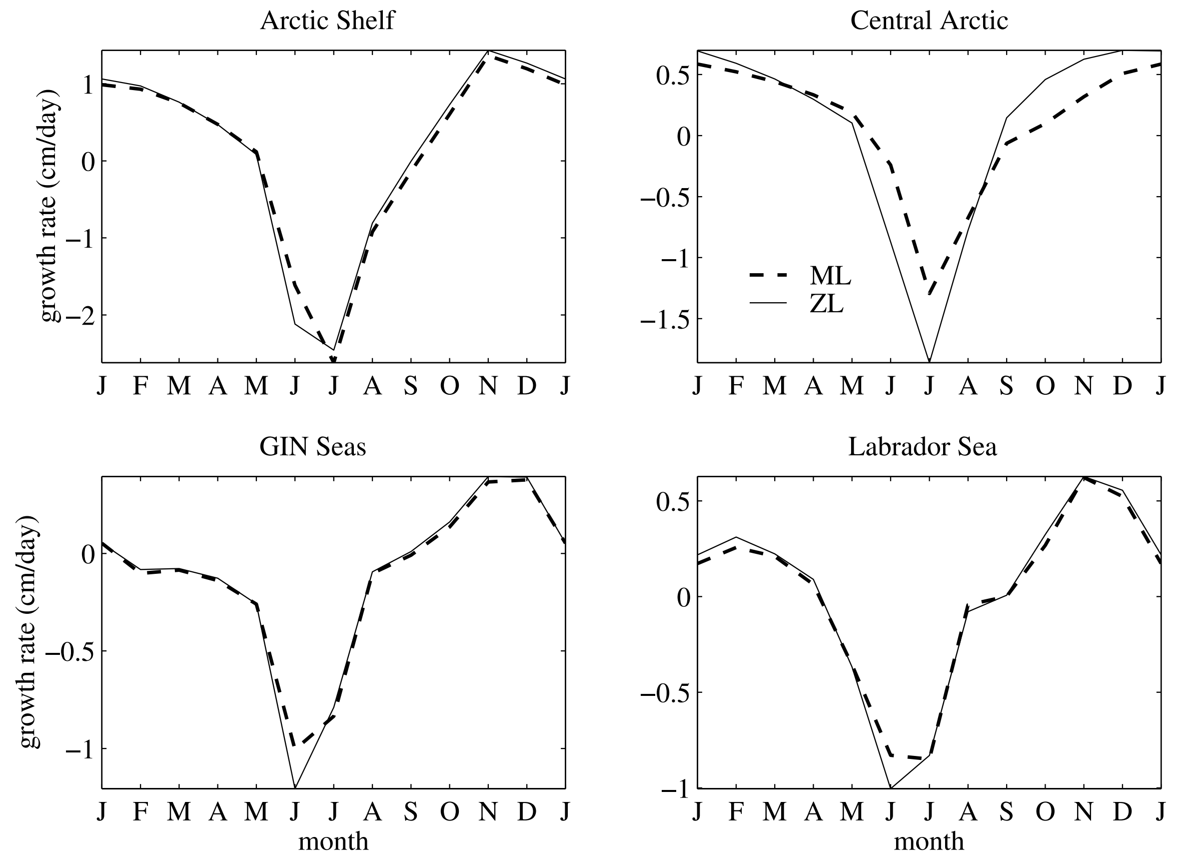

Figure 16. As in Fig. 15 but for growth rates.

t the thickness is roughly 100 cm greater. The pattern resembles the observations from *Bourke and Garrett* [1987] (see 9d) in winter, but the thickness in the central Arctic is $50 - 100$ cm too low. While the basin-scale thickness pattern seems to be improved when C_s is decreased from 0.5 to 0, the thickness with $C_s = 0.5$ compares more favorably to observations in the Beaufort Sea. Compared to the control case with $C_s = 0.5$, the ice thickness in the Beaufort Gyre decreases by as much as 125 cm (see Fig. 18b). The concentration of ice thicker than 500 cm in the western Arctic is about 20% year round (not shown), which is about half as great as in the control case. This quantity compares well with the observation from submarine cruises summarized in Table 2. Thus we conclude that the model produces about the proper concentration of ridged ice when $C_s = 0.$, but the firstyear and multiyear ice are slightly thin compared to observations.

To summarize the oceanic model sensitive to C_s, we show the upper ocean layer salinity difference for cases with $C_s = 0$ minus $C_s = 0.5$ in Fig. 18b. The differences are small everywhere except in the East Siberian Sea where, as noted above, the salinity with an ITD is considerably fresher than the case without an ITD. The case with $C_s = 0$ tends to produce less freshening here because the ice in the Beaufort Gyre is much thinner and there is simply less ice to melt back in the summer. Differences in other variables (e.g., compactness, turbulent heat fluxes, surface air temperature, and meridional overturning) relevant for coupled climate modeling are minor.

It is impractical to test the full spectrum of values for C_s and its interdependence on other variables like e and Z. However, we emphasize that for climate purposes the results are not very sensitive to these variables, because they mainly affect ridged ice production in the Arctic Basin. The concentration of thin ice changes very little despite the decrease in lead opening in the Beaufort Sea because thin ice is transferred to thick categories at a slower rate.

4. Discussion and Conclusion

Typical sea ice models that are currently used in climate studies have one category of ice and Semtner zero-layer style thermodynamics (i.e., much like the two-level

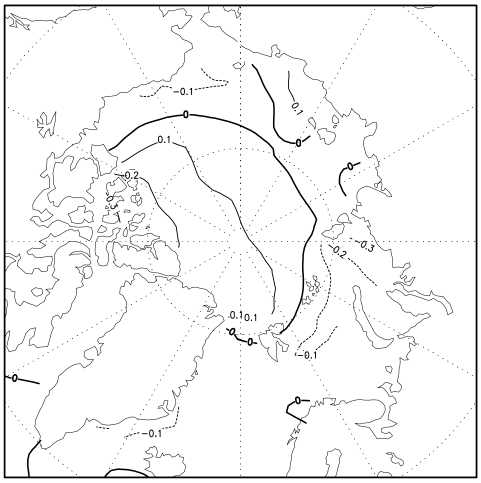

Figure 17. Difference of annual mean upper 25 m ocean salinity for ML-ZL cases. Units are in ‰.

model of *Hibler* [1979]). Our analysis suggests that the addition of multi-layer thermodynamics leads to thicker ice in the central Arctic, especially in summer, but that the compactness changes little. The multi-layer thermodynamics has little affect on the annual mean heat exchange with the atmosphere. However the ocean in the central Arctic responds to significant differences in ice growth and melt rates. The integrated effect of these differences increases the annual mean salinity of the upper ocean in the central Arctic by up to 0.2‰ and freshen some parts of the the shelf region by an equal amount. Ice export through Fram Strait is nearly unchanged as is the thickness and compactness in the GIN Seas, so deep water formation in the northern North Atlantic also changes very little.

If we also add an ice-thickness distribution model, the changes are much more widespread. The ice becomes even thicker, but the pattern depends on parameters that are not well constrained by observations (e.g., C_s, Z, and e). Generally the ice is thicker in regions of strong convergence and shear, such as north of Greenland and the Canadian Archipelago and in the Beaufort Gyre. In the summer, ice compactness is substantially lower everywhere in the Arctic with the exception of the Chukchi and Labrador Sea. The mean latent plus sensible heat flux increases throughout the central Arctic and GIN Seas with a maximum increase in late winter–spring in excess of 15 W m^{-2} in the GIN Seas. Net freezing rates increase by 25-50 cm yr^{-1} over a large part of the central Arctic and decrease accordingly in the east Siberian Sea, Barents Sea, and east of Greenland. Ultimately the ocean salinity increases by about 0.1‰ throughout the central Arctic and GIN Seas and decreases sharply in the Chukchi and East Siberian Seas. The annual mean and standard deviation of ice export through Fram Strait increases by about 30%. As a result, we see a much stronger link

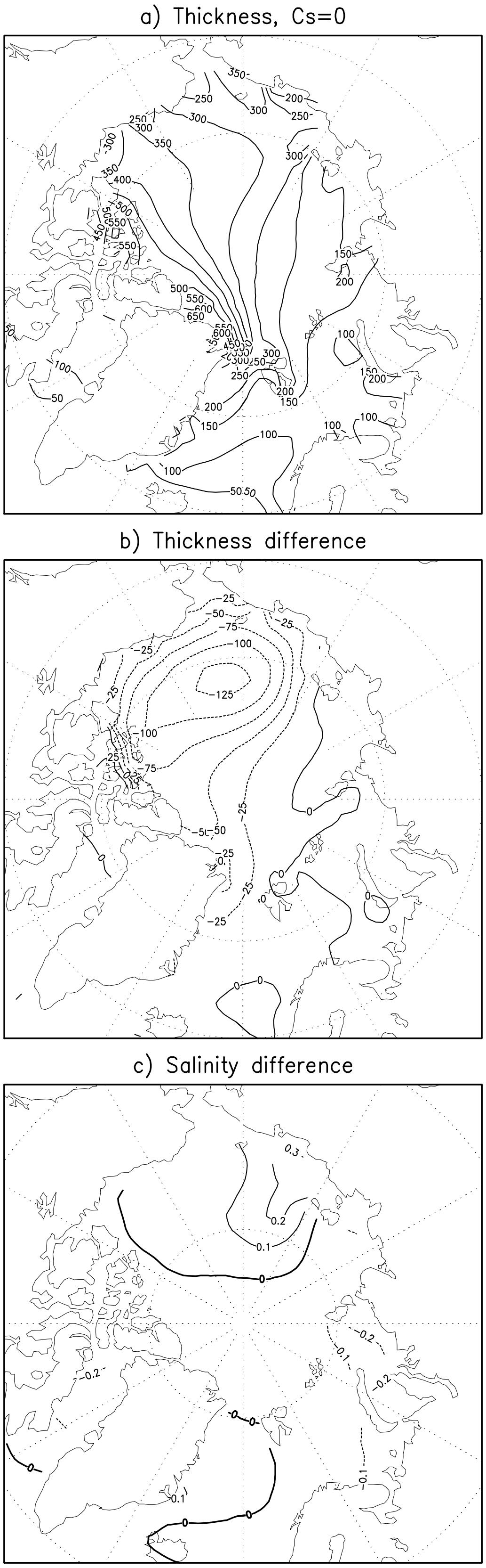

Figure 18. Winter sea ice thickness for case with $C_s = 0$ (a) and winter thickness difference (b) and annual mean salinity difference (c) between cases with $C_s = 0$ minus $C_s = 0.5$. Units are cm for (a) and (b) and ‰ for (c).

between ice thickness in the GIN Seas and the meridional overturning in the North Atlantic Ocean, and the standard deviation of the overturning index increases by about 50%.

We find both of these additions to the typical two-level model are important for climate simulations. The addition of an ice-thickness distribution model yields more dramatic changes in almost every way, except in the salinity of the upper ocean in the central Arctic, where the addition of multi-layer thermodynamics has a stronger influence.

These simulations demonstrate that the Lagrangian thickness distribution model does reasonably well in simulating the mean arctic climate. However, parameters that produced realistic amounts of ridged ice in the Beaufort Gyre in uncoupled simulations [*Flato and Hibler*, 1995], tend to allow too much thick, ridged ice in our coupled simulation. Our effort to reduce the amount of ridged ice production by neglecting ridging from shear deformation improved our simulation of the ice thickness. At this time, observations cannot determine what amount of ridged ice production from shear is correct. It is some consolation that most variables that influence climate are relatively insensitive to the details of the distribution of thick, ridged ice.

Another part of this study involved determining the minimum number of ice thickness categories that are needed for climate studies. Heat and freshwater exchange with the atmosphere and ocean depend on the concentration of open water and thin ice, which is relatively insensitive to the number of categories beyond 5. The ice thickness differs with the number of categories owing to the distribution of thick ice, which has only a modest effect on variables that are relevant for coupled climate modeling. From these tests we conclude that just 5 categories are necessary for properly resolving the seasonal cycle of climatically important variables. However, we caution that the way the categories are defined and the formulation of the ice thickness distribution (e.g., Lagrangian *vs.* Eulerian) can affect this conclusion.

Appendix A: Evaluation of mechanical redistribution and ice strength

The evaluation of mechanical redistribution and ice strength is described for the Lagrangian ice thickness distribution that was used in this study. The mechanical redistribution function Ψ_i in Eq 4 is the integral of the continuous function from Eq. 7 over the thickness limits of each category:

$$\Psi_i = \int_{\hat{H}_{i-1}}^{\hat{H}_i} \Psi dh = \delta(h)\left(\dot{\epsilon}_I + |\dot{\epsilon}|\alpha_r(\theta)\right) + |\dot{\epsilon}|\alpha_r(\theta) W_i, \tag{A1}$$

where $|\dot{\epsilon}| = (\dot{\epsilon}_I^2 + \dot{\epsilon}_{II}^2)^{1/2}$, $\dot{\epsilon}_I$ and $\dot{\epsilon}_{II}$ are strain rate invariants, and $\theta = \tan^{-1}(\dot{\epsilon}_{II}/\dot{\epsilon}_I)$. The W_i factors can be separated into participation and redistribution components

$$W_i = -W_{ai} + W_{ni}, \tag{A2}$$

such that

$$\begin{aligned} W_{ai} =& \frac{1}{\eta}\int_{\hat{H}_{i-1}}^{\hat{H}_i} b(h)g(h)dh \\ W_{ni} =& \frac{1}{\eta}\int_{\hat{H}_{i-1}}^{\hat{H}_i}\int_0^{\hat{H}_i} \gamma(h',h)b(h')g(h')dh'dh \end{aligned} \tag{A3}$$

where $b(h)$ is a weighting function, $\gamma(h',h)$ describes the redistribution process, and η normalizes W_i such that $\sum_{i=0}^{M}\Psi_i = \dot{\epsilon}_I$. As described in section 2.2, we assume a form of b(h) from *Thorndike et al.* [1975]:

$$b(G) = \begin{cases} \frac{2}{G^*}\left[1 - \frac{G(h)}{G^*}\right]; & G \le G^* \\ 0; & G > G^*, \end{cases} \tag{A4}$$

where $G(h) = \int_0^h g(h)dh$ is the cumulative distribution and $G^* = 0.15$. Hence, we find

$$\begin{aligned} W_{ai} =& \frac{1}{\eta}\int_{min(G^*,G_{i-1})}^{min(G^*,G_i)} b(G)dG \\ =& \frac{1}{\eta}(V_{i-1} - V_i), \end{aligned} \tag{A5}$$

where $G_i = \sum_{j=0}^{i} g_j$, with $G_{-1} = 0$, and

$$V_i = \begin{cases} [1 - \frac{G_i}{G^*}]^2; & G_i \le G^* \\ 0; & G_i > G^*. \end{cases} \tag{A6}$$

Using the form of $\gamma(h',h)$ from *Hibler* [1980],

$$W_{ni} = \sum_{j=1}^{i} W_{aj}\Gamma_{j,i}, \tag{A7}$$

where the discrete distributor Γ_{ji} is computed from

$$\Gamma_{ji} = \frac{min(2\sqrt{KH_j}, \hat{H}_i) - max(2H_j, \hat{H}_{i-1})}{2(K - H_j)}, \tag{A8}$$

when $2H_j > \hat{H}_{i-1}$ or $2\sqrt{KH_j} < \hat{H}_i$, and otherwise $\Gamma_{ji} = 0$.

Using the expressions for the W_i factors, the rates of change of the ice and snow volumes due to mechanical redistribution are

$$\begin{aligned} \Theta_i =& |\dot{\epsilon}|\alpha_r(\theta)\Big[-H_i W_{ai} + \sum_{j=1}^{i} \tilde{H}_{ji} W_{aj}\Gamma_{ji}\Big] \\ \Theta_i^s =& |\dot{\epsilon}|\alpha_r(\theta)\Big[-H_i^s W_{ai} + \sum_{j=1}^{i} \tilde{H}_{ji}^s W_{aj}\Gamma_{ji}\Big], \end{aligned} \tag{A9}$$

where

$$\begin{aligned} \tilde{H}_{ji} =& \frac{1}{2}\left[max\left(2H_j, \hat{H}_{i-1}\right) + min\left(2\sqrt{KH_j}, \hat{H}_i\right)\right] \\ \tilde{H}_{ji}^s =& H_j^s \frac{H_j + \sqrt{KH_j}}{H_j}. \end{aligned} \tag{A10}$$

For simplicity, we assume that mechanical redistribution does not mix thermal energy vertically. Hence, the rate of change of the ice energy of melting is

$$\Pi_i(z_i^*) = |\dot{\epsilon}|\alpha_r(\theta)\Big[- q_i(z_i^*)H_i W_{ai} + \sum_{j=1}^{i} q_j(z_j^*)\tilde{H}_{ji} W_{aj}\Gamma_{ji}\Big]. \tag{A11}$$

Data from which to develop a less restrictive model are lacking. Finally, the ice strength is written

$$P = Zc_p \sum_{i=1}^{M}\Big[- H_i^2 W_{ai} + \sum_{j=1}^{i} \tilde{H}_{ji}^2 W_{aj}\Gamma_{ji}\Big]. \tag{A12}$$

Acknowledgments. We thank G. Flato and W. Hibler for helpful discussions. This work was supported by NSERC Strategic, Operating, and Steacie Supplement grants as well as the Atmospheric Environment Service, Canadian Climate Research Network and the Canadian Institute for Climate Studies. All computations were conducted on a suite of IBM RS6000s, including two IBM SP2s that were partially funded by an IBM SUR grant.

References

Aagaard, K., and E. C. Carmack, The role of sea ice and other fresh water in the Arctic circulation, *J. Geophys. Res.*, *94*, 14485–14498, 1989.

Arbetter, T. E., J. A. Curry, and J. A. Maslanik, Effects of rheology and ice thickness distribution in a dynamic-thermodynamic sea ice model, *J. Phys. Oceanogr.*, 1999.

Bitz, C. M., and W. H. Lipscomb, An energy-conserving thermodynamic model of sea ice, *J. Geophys. Res.*, *104*, 15,669–15,677, 1999.

Björk, G., On the response of the equilibrium thickness distribuition of sea ice to ice export, mechanical deformation and thermal forcing with application to the Arctic Ocean, *J. Geophys. Res.*, *97*, 11287–11298, 1992.

Bourke, R. H., and R. P. Garrett, Sea ice thickness distribution in the arctic ocean, *Cold Regions Sci. and Tech.*, *13*, 259–280, 1987.

Cavalieri, D. J., P. Gloerson, C. L. Parkinson, J. C. Comiso, and H. J. Zwally, Observed hemispheric asymmetry in global sea ice changes, *Science*, *278*, 1104–1106, 1997.

Chapman, W. L., and J. E. Walsh, Recent variations of sea ice and air temperature in high latitudes, *Bull. Amer. Meteor. Soc.*, *74*, 33–47, 1993.

Coon, M. D., G. A. Maykut, R. S. Pritchard, D. A. Rothrock, and A. S. Thorndike, Modeling the pack ice as an elastic-plastic material, *AIDJEX Bull.*, *24*, 1–105, 1974.

Curry, J. A., J. L. Schramm, and E. E. Ebert, Sea ice-albedo climate feedback mechanism, *J. Climate*, *8*, 240–247, 1995.

Ebert, E. E., and J. A. Curry, An intermediate one-dimensional thermodynamic sea ice model for investigating ice-atmosphere interactions, *J. Geophys. Res.*, *98*, 10085–10109, 1993.

Eby, M., and G. Holloway, Grid transformation for incorporating the Arctic in a global ocean model, *Clim. Dyn.*, *10*, 241–247, 1994.

Fanning, A., and A. J. Weaver, An atmospheric energy-moisture balance model: Climatology, interpentadal climate change, and coupling to an ocean general circulation model, *J. Geophys. Res.*, *101*, 15,111–15,128, 1996.

Fichefet, T., and M. Morales Maqueda, Sensitivity of a global sea ice model to the treatment of ice thermodynamics and dynamics, *J. Geophys. Res.*, *102*, 12609–12646, 1997.

Flato, G. M., and W. D. Hibler III, Ridging and strength in modelling the thickness distribution of Arctic sea ice, *J. Geophys. Res.*, *C9*, 18611–18626, 1995.

Häkkinen, S., and G. L. Mellor, Modeling the seasonal variability of a coupled Arctic ice-ocean system, *J. Geophys. Res.*, *97*, 20285–20304, 1992.

Hibler III, W. D., A dynamic thermodynamic sea ice model, *J. Phys. Oceanogr.*, *9*, 815–846, 1979.

Hibler III, W. D., Modeling a variable thickness ice cover, *Mon. Wea. Rev.*, *108*, 1943–1973, 1980.

Holland, D. M., L. A. Mysak, D. K. Manak, and J. M. Oberhuber, Sensitivity study of a dynamic thermodynamic sea ice model, *J. Geophys. Res.*, *98*, 2561–2586, 1993.

Holland, M. M., C. Bitz, M. Eby, and A. Weaver, Low frequency variability of the North Atlantic/Arctic climate system in a coupled ocean-sea ice-atmosphere model, *J. Climate*, submitted 1999.

Hopkins, M. A., and W. D. Hibler III, On the ridging of a thin sheet of lead ice, *Annals of Glaciology*, *15*, 81–86, 1991.

Hunke, E. C., and J. K. Dukowicz, An elastic-viscous-plastic model for sea ice dynamics, *J. Phys. Oceanogr.*, *27*, 1849–1867, 1997.

Hurrell, J. W., Decadal trends in the North Atlantic Oscillation: Regional temeperatures and preciptiation, *Science*, *269*, 676–679, 1995.

Kalnay, E., et al., The NCEP/NCAR 40-year reanalysis project, *Bull. Amer. Meteor. Soc.*, *77*, 437–471, 1996.

Kwok, R., and D. A. Rothrock, Variability of Fram Strait ice flux and North Atlantic Oscillation, *J. Geophys. Res.*, *104*, 5,177–5,189, 1999.

Manabe, S., and R. J. Stouffer, Sensitivity of a global climate model to an increase of CO_2 concentration in the atmosphere, *J. Geophys. Res.*, *85*, 5529–5554, 1980.

Maykut, G. A., Large-scale heat exchange and ice production in the central Arctic, *J. Geophys. Res.*, *87*, 7971–7984, 1982.

Maykut, G. A., and D. Perovich, The role of shortwave radiation in the summer decay of a sea ice cover, *J. Geophys. Res.*, *92*, 7032–7044, 1987.

Maykut, G. A., and N. Untersteiner, Some results from a time-dependent thermodynamic model of sea ice, *J. Geophys. Res.*, *76*, 1550–1575, 1971.

McLaren, A. S., The under-ice thickness distribution of the Arctic Basin as recorded in 1958 and 1970, *J. Geophys. Res.*, *94*, 4971–4983, 1989.

McPhee, M. G., Turbulent heat flux in the upper ocean under sea ice, *J. Geophys. Res.*, *97*, 5365–5379, 1992.

Pacanowski, R. C., The GFDL modular ocean model documentation, user's and reference manual, Tech. Rep. The GFDL Ocean Group Tech. Rep. 3.2, pp. 329, Geophys. Fluid Dyn., Princeton, New Jersey, 1996.

Rigor, I., Variations in surface air temperatures over the Arctic Ocean from 1979-1997, *J. Climate*, submitted 1998.

Rothrock, D. A., The energetics of the plastic deformation of pack ice by ridging, *J. Geophys. Res.*, *80*, 4514–4519, 1975.

Rothrock, D. A., Ice thickness distribution-measurement and theory, in *The Geophysics of Sea Ice*, edited by N. Untersteiner, vol. 146, pp. 551–575, NATO ASI Series B, Physics, Plenum, New York, London, 1986.

Rothrock, D. A., and A. S. Thorndike, Measuring the sea ice floe size distribution, *J. Geophys. Res.*, *89*, 6477–6486, 1984.

Schramm, J. L., M. M. Holland, and J. A. Curry, Modeling the thermodynamics of a distribution of sea ice thicknesses. Part I Model description and validation, *J. Geophys. Res.*, *102*, 23,079–23,091, 1997.

Schwarzacher, W., Pack ice studies in the Arctic Ocean, *J. Geophys. Res.*, *64*, 2357–2367, 1959.

Semtner, A. J., A model for the thermodynamic growth of sea ice in numerical investigaions of climate, *J. Phys. Oceanogr.*, *6*, 379–389, 1976.

Steele, M., Sea ice melting and floe geometry in a simple ice-ocean model, *J. Geophys. Res.*, *97*, 17,729–17,738, 1992.

Steele, M., and G. M. Flato, Sea ice growth, melt, and modeling: A survey, in *The Arctic Ocean Freshwater Budget*, NATO ARW Volume, Plenum, New York, London, 1999.

Stern, H. L., D. A. Rothrock, and R. Kwok, Open water production in arctic sea ice: satellite measurements and model parameterizations, *J. Geophys. Res.*, *100*, 20,601–20,612, 1995.

Thorndike, A. S., D. S. Rothrock, G. A. Maykut, and R. Colony, The thickness distribution of sea ice, *J. Geophys. Res.*, *80*, 4501–4513, 1975.

Tucker III, W. B., and J. W. Govoni, Morphological investigations of firstyear sea ice pressure ridge sails, *Cold Reg. Sci. Technol.*, *5*, 1–12, 1981.

Vinje, T., N. Nordlund, and A. Kvambekk, Monitoring ice thickness in Fram Strait, *J. Geophys. Res.*, *103*, 10,437–10,449, 1998.

Wadhams, P., The seasonal ice zone, in *The Geophysics of Sea Ice*, edited by N. Untersteiner, vol. 146, pp. 825–991, NATO ASI Series B, Physics, Plenum, New York, London, 1986.

Wadhams, P., Evidence for thinning of the Arctic ice cover north of Greenland, *Nature*, *345*, 795–797, 1990.

Wadhams, P., Sea ice thickness distribution in the greenland sea and eurasian basin, *J. Geophys. Res.*, *97*, 5331–5348, 1992.

Wadhams, P., and R. J. Horne, An analysis of ice profiles obtained by submarine sonar in the Beaufort Sea, *J. Glac.*, *25*, 401–424, 1980.

Walsh, J. E., W. L. Chapman, and T. L. Shy, Recent decrease of sea level pressure in the central Arctic, *J. Climate*, *9*, 480–486, 1996.

WCRP, Arctic Climate System Study (ACSYS) initial implementation plan, Tech. rep., WCRP-85, WMO/IT-No. 627, 1994.

Zhang, J., and W. D. Hibler III, On an efficient numerical method for modeling sea ice dynamics, *J. Geophys. Res.*, *102*, 8691–8702, 1997.

C. M. Bitz, Quaternary Research Center, MS 351360, University of Washington, Seattle, WA 98195-1360. (bitz@atmos.washington.edu)

M. M. Holland, NCAR.

This preprint was prepared with AGU's LaTeX macros v5.01, with the extension package 'AGU^{++}' by P. W. Daly, version 1.5b from 1996/10/24.